Linking inherent anisotropy with liquefaction phenomena of granular materials by means of DEM analysis

HOSTED BY

ELSEVIER

Available online at www.sciencedirect.com

ScienceDirect

Soils and Foundations 62 (2022) 101202

SOILS AND FOUNDATIONS

www.elsevier.com/locate/sandf

Technical Paper

Linking inherent anisotropy with liquefaction phenomena of granular materials by means of DEM analysis

Masahide Otsubo [a,*], Sanjei Chitravel [a], Reiko Kuwano [a], Kevin J. Hanley [b], Hiroyuki Kyokawa [c], Junichi Koseki [c]

[a] *Institute of Industrial Science, The University of Tokyo, 4-6-1 Komaba, Meguro-ku, Tokyo 153-8505, Japan*
[b] *School of Engineering, Institute for Infrastructure and Environment, The University of Edinburgh, Edinburgh EH9 3JL, UK*
[c] *Department of Civil Engineering, The University of Tokyo, 7-3-1 Hongo, Bunkyo-ku 113-8654, Japan*

Received 24 March 2022; received in revised form 25 June 2022; accepted 19 July 2022

Abstract

The liquefaction phenomena of sands have been studied by many researchers to date. Laboratory element tests have revealed key factors that govern liquefaction phenomena, such as relative density, particle size distribution, and grain shape. However, challenges remain in quantifying inherent anisotropy and in evaluating its impact on liquefaction phenomena. This contribution explores the effect of inherent anisotropy on the mechanical response of granular materials using the discrete element method. Samples composed of spherical particles are prepared which have approximately the same void ratio and mean coordination number (*CN*), but varying degrees of inherent anisotropy in terms of contact normals. Their mechanical responses are compared under drained and undrained triaxial monotonic loading as well as under undrained cyclic loading. The simulation results reveal that cyclic instability followed by liquefaction can be observed for loose samples having a large degree of inherent anisotropy. Since a sample having initial anisotropy tends to deform more in its weaker direction, leading to lower liquefaction resistance, a sample having an isotropic fabric potentially exhibits the greatest liquefaction resistance. Moreover, the effective stress path during undrained cyclic loading is found to follow the instability and failure lines observed for static liquefaction under undrained monotonic loading. From a micromechanical perspective, the recovery of effective stress during liquefaction can be observed when a threshold *CN* develops along with the evolving induced anisotropy. Realising that the conventional index of the anisotropic degree (a) is not effective when the *CN* drops to almost zero during cyclic liquefaction, this contribution proposes an alternative index, *effective anisotropy* ($a \times CN$), with which the evolution of induced anisotropy can be tracked effectively, and common upper and lower bounds can be defined for both undrained monotonic and cyclic loading tests.

Keywords: Liquefaction; Discrete element method; Anisotropy; Fabric; Triaxial tests

1. Introduction

The liquefaction of granular soil can cause severe damage to infrastructure. Intense research on the liquefaction of sands began after the Niigata and Alaska earthquakes of 1964 (*e.g.*, Seed and Idriss, 1967; McCulloch and Bonilla, 1970; Ishihara and Koga, 1981), and accelerated after the 2011 off the Pacific coast of Tohoku Earthquake (*e.g.*, Sasaki et al., 2012). Liquefaction refers to the situa-

Peer review under responsibility of The Japanese Geotechnical Society.
* Corresponding author at: Public Works Research Institute, 1-6 Minamihara, Tsukuba, Ibaraki, 305-8516, Japan
E-mail addresses: otsubo@iis.u-tokyo.ac.jp, ootsubo-m573cm@pwri.go.jp (M. Otsubo), sanjei9@iis.u-tokyo.ac.jp (S. Chitravel), kuwano@iis.u-tokyo.ac.jp (R. Kuwano), K.Hanley@ed.ac.uk (K.J. Hanley), kyokawa@civil.t.u-tokyo.ac.jp (H. Kyokawa), koseki@civil.t.u-tokyo.ac.jp (J. Koseki).

https://doi.org/10.1016/j.sandf.2022.101202
0038-0806/

Nomenclature

a	Anisotropic degree
a_0	Initial anisotropic degree
C_u	Uniformity coefficient
CN	Mean coordination number
CN_0	Initial mean coordination number
CN^*	Mean mechanical coordination number
D	Diameter of a sphere
D_{50}	Median diameter of spheres
D_{r0}	Initial relative density
e	Void ratio
e_0	Initial void ratio
e^*	Mechanical void ratio
e_{min}	Minimum void ratio of a sample
e_{max}	Maximum void ratio of a sample
E	Young's modulus of a sphere
ε_a	Axial strain during loading
ε_{DA}	Double amplitude axial strain during loading
ε_{vol}	Volumetric strain during loading
$\Delta\varepsilon_h$	Horizontal strain during sample preparation
$\Delta\varepsilon_v$	Vertical strain during sample preparation
φ_h	Horizontal component of fabric tensor
φ_{h0}	Horizontal component of initial fabric tensor
φ_v	Vertical component of fabric tensor
φ_{v0}	Vertical component of initial fabric tensor
G	Shear modulus of a sphere
G_s	Specific gravity of a sphere
G_{0h}	Small-strain shear modulus of a sample measured in the horizontal direction
G_{0v}	Small-strain shear modulus of a sample measured in the vertical direction
K	Stress ratio ($= \sigma'_h/\sigma'_v$) at sample preparation
μ_{prep}	Inter-particle friction coefficient during sample preparation
μ_{load}	Inter-particle friction coefficient during loading
N_c	Total number of contacts
N_p	Total number of particles
P'	Mean effective stress ($= [\sigma'_v + 2\ \sigma'_h]/3$)
p'_0	Initial isotropic effective stress ($= 100$ kPa)
q	Deviator stress ($= \sigma'_v - \sigma'_h$)
σ'_h	Principal stress in the horizontal direction
σ'_v	Principal stress in the vertical direction
v	Poisson's ratio of a sphere
CSR	Cyclic stress ratio ($= q/2p'_0$)
FL	Failure line during undrained loading
Hor	Sample prepared having an anisotropic fabric preferentially in the horizontal plane
IL	Instability line during undrained loading
Iso	Sample prepared having an isotropic fabric
NL	Number of cycles to liquefaction when ε_{DA} reaches 2%
PSD	Particle size distribution
Ver	Sample prepared having an anisotropic fabric preferentially in the vertical direction

tion in which the effective stress becomes zero (Seed and Lee, 1966). In terms of laboratory element tests, liquefaction can be divided into two categories: static liquefaction and cyclic liquefaction induced by undrained monotonic and cyclic loading, respectively (Ishihara, 1993). Static liquefaction, observed for loose samples, is characterised by strain-softening behaviour with an abrupt loss of strength, leading to flow deformation (Yamamuro and Lade, 1997; Chu and Leong, 2001). Cyclic liquefaction is accompanied by either cyclic instability or cyclic mobility for loose or denser sands, respectively (Castro, 1975; Casagrande, 1976).

The liquefaction resistance of a given material is influenced by not only relative density and confining pressure, but also inherent anisotropy, *i.e.*, the initial soil fabric (Tatsuoka et al., 1986). Here, the soil fabric refers to the geometric arrangement of the particles and pore spaces. Different sample preparation methods induce different degrees of inherent anisotropy in soil samples (Tatsuoka et al., 1986; Vaid et al., 1999; Ishibashi and Capar, 2003; Sze and Yang, 2014). Due to technical limitations, only a few studies found in the literature have quantified the anisotropy of prepared samples using microscopic methods (Oda, 1972; Suzuki and Suzuki, 1988; Yang et al., 2008; Ni et al., 2021). Yang et al. (2008) and Sze and Yang (2014) found that samples prepared by moist tamping (MT) have a random arrangement of sand particles, leading to a lower degree of inherent anisotropy than samples prepared by dry deposition (DD).

Numerous studies have been carried out to understand the effect of the various sample preparation methods on the cyclic liquefaction of sands under different densities and confining pressures (*e.g.*, Miura and Toki, 1982; Tatsuoka et al., 1986; Yamashita and Toki, 1993; Ishibashi and Capar, 2003; Sze and Yang, 2014; Ni et al., 2021). For example, Tatsuoka et al. (1986) concluded that the MT method tends to provide greater liquefaction resistance than the air-pluviation (AP) method; similar observations were reported by other researchers (*e.g.*, Miura and Toki, 1982; Yamashita and Toki, 1993; Ishibashi and Capar, 2003; Sze and Yang, 2014).

The discrete element method (DEM) is a powerful numerical tool for understanding the particle-scale micromechanics of granular soil and for assisting in the interpretation of equivalent experimental results. DEM enables the quantification of soil fabrics in terms of the

contact normals, which helps with the interpretation of the overall response of granular materials as pioneered by Oda (1982). This allows researchers to quantify *inherent anisotropy* under the initial isotropic stress state and to track the evolution of *induced anisotropy* subjected to changes in the stress state. The importance of inherent anisotropy on the shear behaviour of granular soil has been reported in the literature (*e.g.*, Yimsiri and Soga, 2010; Dai et al., 2016). Some recent studies have explored the relation between fabric anisotropy and undrained cyclic loading behaviour using a 2D DEM (Wang and Wei, 2016) and a 3D DEM (Wei and Wang, 2017). Wei et al. (2018) found that a highly anisotropic sample induced by pre-shearing has a lower liquefaction resistance.

As discussed above, laboratory element tests have revealed key factors that govern liquefaction phenomena. However, challenges remain in quantifying inherent anisotropy and in evaluating its impact on liquefaction phenomena. Building on the earlier works of Yimsiri and Soga (2010), Wei et al. (2018), among others, this contribution explores the effect of inherent anisotropy on the mechanical response of granular materials using DEM. Samples having varying degrees of inherent anisotropy are prepared at approximately the same void ratio and mean coordination number, and their mechanical responses, in relation to their induced anisotropy, are discussed under drained and undrained triaxial monotonic loading as well as under undrained cyclic loading.

2. Sample preparation and inherent anisotropy

2.1. Material properties

The present study uses spherical particles to investigate the fundamental effect of inherent anisotropy on the mechanical response of granular materials where the complicating effect of particle shape has been removed. The material properties of the tested spherical particles are similar to the typical properties of glass beads (Young's modulus (E): 71.6 GPa, shear modulus (G): 29.1 GPa, Poisson's ratio (ν): 0.23, and specific gravity (G_s): 2.7). Particle diameters (D) range from 1.2 mm to 2.2 mm (Fig. 1) with a median size (D_{50}) of 1.89 mm and coefficient of uniformity (C_u) of 1.37, which represent a uniformly graded sand. A simplified Hertz-Mindlin contact model was used for the interaction between particles, since the contact stiffness is automatically determined and updated as a function of the particle properties and the applied load between two spherical particles (see Morimoto et al. (2021) for a more detailed explanation). A modified version of LAMMPS (Large-scale Atomic/Molecular Massively Parallel Simulator) (Plimpton, 1995) was used to run these DEM simulations. The time increment used in the present simulations was 4×10^{-7} s to satisfy the critical time increment for the given material (Otsubo et al., 2017).

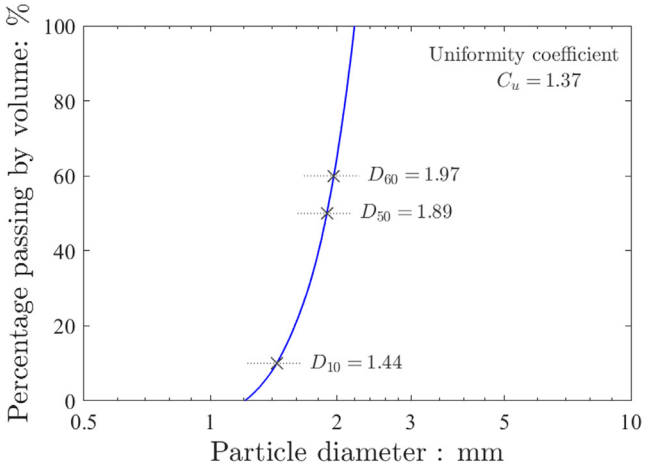

Fig. 1. Particle size distribution (PSD) of tested spherical particles.

2.2. Preparation method for Iso-, Ver-, and Hor-series samples

The sample preparation method adopted in this study follows the three steps illustrated in Fig. 2. Firstly, a cloud of 30,000 spherical particles was generated randomly in a cuboidal space without allowing the particles to touch each other. Periodic boundaries were used for the three principal directions. Secondly, three different initial compression procedures were employed to prepare the *Iso*, *Ver,* and *Hor* samples, respectively, in the absence of gravity, as follows:

- *Iso*: Isotropic compression was applied in the principal directions (x, y, and z) to achieve an isotropic effective stress of $\sigma'_x{=}\sigma'_y{=}\sigma'_z = 100$ kPa (*i.e.*, $p'_0 = 100$ kPa).
- *Ver*: Vertical compression was applied in the z-direction to achieve $\sigma'_z = 1$ kPa ($\sigma'_v = 1$ kPa), while the incremental axial strain in the x- and y- (horizontal) directions was kept at zero, *i.e.*, $\Delta\varepsilon_x{=}\Delta\varepsilon_y = 0$ ($\Delta\varepsilon_h = 0$).
- *Hor*: Horizontal compression was applied in the x- and y-directions to achieve $\sigma'_x{=}\sigma'_y = 1$ kPa ($\sigma'_h = 1$ kPa), while the incremental axial strain in the vertical direction was kept at zero, *i.e.*, $\Delta\varepsilon_z = 0$ ($\Delta\varepsilon_v = 0$).

Thirdly, for the *Ver* and *Hor* samples, further compression was then applied to achieve $\sigma'_x{=}\sigma'_y{=}\sigma'_z = 100$ kPa ($p'_0 = 100$ kPa). In the sample preparation stage, a maximum strain rate of 0.2 [s^{-1}] was used and the strain rate was reduced from this maximum value as the desired stress was approached, as described in Otsubo (2016). The above process used an inter-particle friction coefficient during the sample preparation (μ_{prep}). Referring to Table 1, slightly different μ_{prep} values of around 0.15 were used to prepare loose samples, resulting in similar initial void ratios ($e_0 = 0.643$–0.645). The initial mean coordination number (CN_0), *i.e.*, the number of contact points per particle, was also similar among the three samples ($CN_0 = 4.68$–4.69). The above-mentioned loose samples are referred to here

Ⅰ) Particle generation

Generation of 30,000 particles without overlap in absence of gravity

Ⅱ-a) *Iso*-, *Ver*- and *Hor-series* samples

Iso : Compression to $\sigma_x'=\sigma_y'=\sigma_z'=$ 100 kPa
Ver : 1-D vertical compression to $\sigma_z'=$ 1 kPa while keeping $\Delta\varepsilon_x=\Delta\varepsilon_y=0$ (*i.e.*, $\Delta\varepsilon_h=0$)
Hor : Horizontal compression to $\sigma_x'=\sigma_y'=$ 1 kPa while keeping $\Delta\varepsilon_z=0$ (*i.e.*, $\Delta\varepsilon_v=0$)

Ⅱ-b) *K*-series samples

Compression to specified $K=\sigma_h'/\sigma_v'$ where major principal stress is 1 kPa
Note: $\sigma_v'=\sigma_z'$, $\sigma_h'=(\sigma_x'+\sigma_y')/2$

Ⅲ) Further compression

Further compression to $\sigma_x'=\sigma_y'=\sigma_z'=$ 100 kPa (*i.e.*, $p_0'=$ 100 kPa)

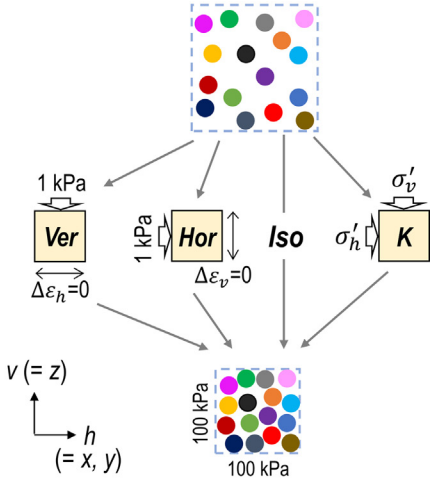

Fig. 2. Sample preparation method adopted in this study.

Table 1
Specifications of sample types and properties of *Iso*, *Hor*, and *Ver*-series samples at $p_0'=100$ kPa.

Sample	μ_{prep}	μ_{load}	e_0	e_0^*	D_{r0} [%]†	CN_0	CN_0^*	φ_{v0}	φ_{h0}	$\varphi_{v0}-\varphi_{h0}$	$\varphi_{v0}/\varphi_{h0}$	a_0
Iso-L	0.150	0.4	0.644	0.753	29.6	4.69	5.19	0.333	0.333	0.000	0.999	−0.002
Ver-L	0.147	0.4	0.643	0.745	30.3	4.68	5.19	0.351	0.324	0.027	1.083	0.097
Hor-L	0.151	0.4	0.645	0.745	29.3	4.69	5.20	0.316	0.342	−0.025	0.926	−0.098
Iso-M	0.055	0.4	0.600	0.661	60.9	5.30	5.67	0.333	0.334	−0.001	0.997	−0.004
Iso-D	0.001	0.4	0.544	0.584	100.0	5.85	6.13	0.332	0.334	−0.002	0.995	−0.007
Iso-e_{max}	0.400	–	0.686	0.884	0.0	3.92	4.61	0.333	0.334	−0.001	0.998	−0.003

† $D_{r0}=(e_{max}-e_0)/(e_{max}-e_{min})\times 100$ [%] where e_{max} and e_{min} correspond to e_0 of the *Iso-e_{max}* and *Iso-D* samples, respectively.

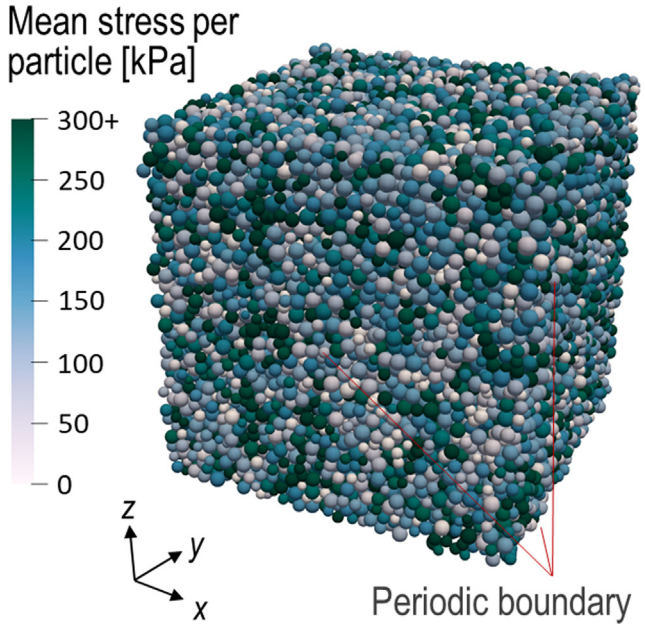

Fig. 3. Representative DEM sample (*Iso-L*) at $p_0'=100$ kPa with periodic boundaries (colour bar shows mean stress per particle).

as *Iso-L*, *Ver-L*, and *Hor-L*. Fig. 3 shows the *Iso-L* sample where the colour of each particle indicates the mean stress per particle, as defined in Morimoto et al. (2021). In this study, a medium dense (*Iso-M*) sample and a dense (*Iso-D*) sample of the *Iso*-series were prepared using lower μ_{prep} of 0.055 and 0.001, respectively (Table 1), to investigate the effect of the initial density on the mechanical response during undrained cyclic loading.

To measure the relative density, the minimum and maximum void ratios (e_{min} and e_{max}) were defined following the method proposed in Salot et al. (2009). Specifically, e_{min} was obtained by setting a small value for μ_{prep} (= 0.001) in the preparation method of the *Iso*-series samples to represent the maximum possible density, *i.e.*, identical to the *Iso-D* sample. e_{max} was obtained by setting $\mu_{prep}=0.4$, the same value used for the subsequent triaxial loading tests (μ_{load}); the prepared sample with $e_{max}=0.686$ is listed in Table 1 as the *Iso-e_{max}* sample for completeness. Therefore, the measured e_0 values are equivalent to $D_{r0}=29.3\%$–30.3% for the loose samples, $D_{r0}=60.9\%$ for the *Iso-M* sample, and $D_{r0}=100\%$ for the *Iso-D* sample, where $D_{r0}=(e_{max}-e_0)/(e_{max}-e_{min})\times 100$ [%].

2.3. Preparation method for K-series samples

To vary the degree of inherent anisotropy in a systematic manner, ten additional loose samples ($D_{r0}=29.0\%$–30.3%) were prepared (referred to here as *K*-series), as follows (Fig. 2):

Table 2
Specifications of sample types and properties of *K*-series samples at $p'_0 = 100$ kPa.

Sample	μ_{prep}	μ_{load}	e_0	e_0^*	D_{r0} [%]	CN_0	CN_0^*	φ_{v0}	φ_{h0}	$\varphi_{v0} - \varphi_{h0}$	$\varphi_{v0}/\varphi_{h0}$	a_0
*K*0.75-*L*	0.176	0.4	0.643	0.742	30.3	4.68	5.14	0.346	0.327	0.019	1.058	0.070
*K*0.80-*L*	0.167	0.4	0.644	0.744	29.5	4.69	5.16	0.341	0.329	0.012	1.036	0.044
*K*0.85-*L*	0.162	0.4	0.645	0.749	29.2	4.69	5.18	0.338	0.331	0.006	1.019	0.023
*K*0.90-*L*	0.158	0.4	0.645	0.751	29.0	4.69	5.18	0.335	0.333	0.002	1.006	0.008
*K*1.00-*L*	0.156	0.4	0.645	0.753	29.2	4.69	5.19	0.334	0.333	0.001	1.002	0.003
*K*1.10-*L*	0.158	0.4	0.645	0.751	29.0	4.69	5.18	0.331	0.334	−0.003	0.991	−0.011
*K*1.20-*L*	0.163	0.4	0.645	0.749	29.2	4.69	5.18	0.328	0.336	−0.007	0.978	−0.028
*K*1.25-*L*	0.165	0.4	0.644	0.742	30.0	4.69	5.16	0.326	0.337	−0.012	0.966	−0.044
*K*1.30-*L*	0.170	0.4	0.644	0.744	29.9	4.68	5.15	0.323	0.339	−0.016	0.953	−0.061
*K*1.35-*L*	0.175	0.4	0.644	0.741	29.6	4.69	5.14	0.320	0.340	−0.020	0.940	−0.078

- *K*-series: A cloud of 30,000 spherical particles was compressed to achieve a specific $K\,(=\sigma'_h/\sigma'_v)$ where the target major principal stress was 1 kPa, *i.e.*, the larger stress component, either σ'_v or σ'_h, was adjusted to 1 kPa while keeping $\sigma'_x{=}\sigma'_y$ $(=\sigma'_h)$. Then, further compression was applied to achieve $p'_0 = 100$ kPa.

Table 2 summarises the properties of the *K*-series samples at $p'_0 = 100$ kPa where the sample name indicates the *K* value at 1 kPa ranging from 0.75 to 1.35. For example, the *K*0.80-*L* sample was compressed initially at $\sigma'_v = 1.0$ kPa and $\sigma'_h = 0.8$ kPa prior to the following compression to $p'_0 = 100$ kPa. The e_0 and CN_0 for the *K*-series samples were equivalent to those for the *Iso*-*L*, *Ver*-*L*, and *Hor*-*L* samples. The simulation results using the *K*-series samples are discussed in Section 5.3. This preparation method is similar to the so-called pre-shear method (*e.g.*, Yimsiri and Soga, 2010; Wei and Wang, 2017) with the main difference being that the resultant CN_0 values are almost identical: $CN_0 = 4.68$–4.69 at $e_0 = 0.643$–0.644 in this study, compared to $CN_0 = 2.51$–3.77 at $e_0 = 0.611$–0.612 in Wei and Wang (2017).

2.4. Quantifying inherent anisotropy

To characterise the difference in packing properties, the second-order fabric tensor φ_{ij}, in terms of contact normal orientations (Satake, 1982; Yimsiri and Soga, 2010), was quantified as:

$$\varphi_{ij} = \frac{1}{N_c}\sum_{N_c} n_i n_j \tag{1}$$

where N_c is the total number of contact points, and n_i and n_j are the contact normals in the *i*- and *j*-directions, respectively ($i, j = x, y, z$). The principal components of the fabric tensor (φ_{xx}, φ_{yy}, and φ_{zz}) were used to quantify the vertical and horizontal components as $\varphi_v = \varphi_{zz}$ and $\varphi_h{=}\ (\varphi_{xx} + \varphi_{yy})/2$, where $\varphi_v + 2\varphi_h = 1$. Following Yimsiri and Soga (2010), the anisotropic degree (a) that expresses the fabric tensor as a single scalar was computed as:

$$a = \frac{5(3\varphi_v - 1)}{5\varphi_v + 1} \tag{2}$$

A larger a (>0) means more contacts in the vertical direction, while a smaller a (<0) means more contacts in the horizontal plane. The initial anisotropic degree (a_0) values at $p'_0 = 100$ kPa for all the tested cases are listed in Tables 1 and 2. For example, the a_0 for *Hor*-*L*, *Iso*-*L*, and *Ver*-*L* are −0.098, −0.002, and 0.097, respectively (Fig. 4). Yimsiri and Soga (2010) prepared samples having $a_0 = -0.13$, −0.01, and 0.12 for the dense case, and $a_0 = -0.04$, 0.01, and 0.06 for the loose case where positive values for the a_0 in DEM correspond to the samples prepared experimentally by the DD or AP method. In a separate study by the authors, using the same material adopted in this paper, a sample was prepared using the AP method, resulting in $a_0 = 0.083$, which is slightly smaller than that for the *Ver*-*L* sample ($a_0 = 0.097$). Sze and Yang (2014) reported that, based on experiments, the MT method can create more isotropic fabric, which is similar to the *Iso*-series samples. Regarding the *Hor*-*L* sample, while its inherent anisotropy may be different from typical samples prepared in experiments, this fundamental study will help in understanding the results of some elaborate experiments where soil fabrics are controlled systematically (*e.g.*, Oda, 1972; Oda et al., 2001). Referring to Table 2, the *K*-series samples cover a range of a_0 from −0.078 to 0.070, which fills the gap of the a_0 values between the *Hor*-*L* and *Ver*-*L* samples. It is noteworthy that samples with even more extreme a_0 values are difficult to prepare using the adopted sample preparation method where specific e_0 and CN_0 values are required. Previous research found in the literature used alternative indices, such as $\varphi_{v0} - \varphi_{h0}$ or $\varphi_{v0}/\varphi_{h0}$ instead of a_0, where a_0 is linearly related to these indices within the range considered in this study ($-0.1 < a_0 < 0.1$).

3. Test methods and definition of parameters

Three loading methods were applied to samples at $p'_0 = 100$ kPa: drained monotonic loading (triaxial compression or extension), undrained monotonic loading (triaxial compression or extension), and undrained cyclic loading. Strain-controlled loading was applied by moving boundaries at 0.0002 m/s, giving a strain rate of approxi-

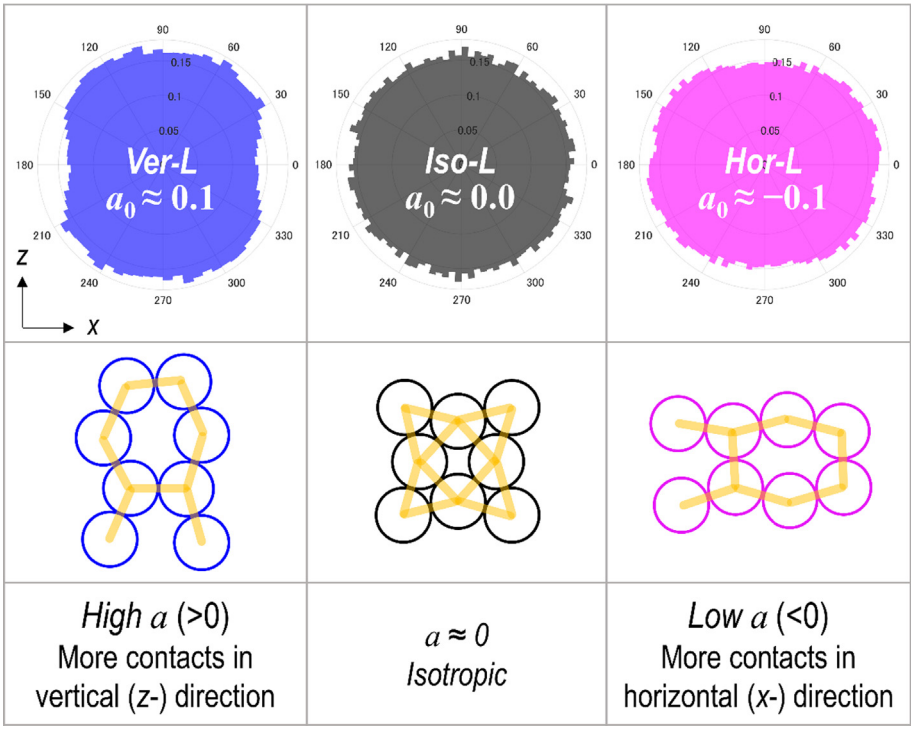

Fig. 4. Orientation of contact normal vectors of *Ver-L*, *Iso-L*, and *Hor-L* samples with schematic illustration of anisotropic degree (a).

mately 0.0039 [s^{-1}]. This strain rate satisfies the quasi-static flow condition for the given material properties at $p'_0 = 100$ kPa (Lopera Perez et al., 2016). During the loading, a local damping coefficient of 0.2 was applied as employed by Morimoto et al. (2021). The μ_{prep} was increased to μ_{load} (= 0.4) for all the simulations during loading.

3.1. Drained monotonic loading

Drained monotonic loading was applied vertically while keeping the lateral effective stress (σ'_h) constant. The deviator stress ratio (q/p') is defined as the ratio between the deviator stress ($q = \sigma'_v - \sigma'_h$) and the mean effective stress ($p' = [\sigma'_v + 2\sigma'_h]/3$), where $q > 0$ for compression and $q < 0$ for extension. During drained monotonic loading, the volumetric strain (ε_{vol}) was calculated from the change in sample bulk volume, where $\varepsilon_{vol} < 0$ for dilation and $\varepsilon_{vol} > 0$ for contraction.

3.2. Undrained monotonic loading

Undrained monotonic loading was simulated by maintaining the sample volume during loading, *i.e.*, the constant volume approach. In physical experiments, excess pore water pressure develops in saturated soil and, in turn, p' decreases when the sample tends to contract, whereas in the constant volume approach, the decrease in p' is caused by the drop in individual particle stress. Details of the mean stress calculation are provided in Morimoto et al. (2021). Finn and Vaid (1977) and Monkul et al. (2015) found similar results for the two different approaches in their experiments. Ng and Dobry (1994) confirmed the capability of DEM to capture the cyclic liquefaction phenomena in granular soil. Bonilla (2004) reported qualitatively similar results between the constant volume approach and undrained loading with fluid coupling using a 2D DEM.

3.3. Undrained cyclic loading

Undrained cyclic loading tests were performed to quantify the liquefaction resistance and the relationship between the cyclic stress ratio (CSR) and the number of cycles to liquefaction (NL). CSR is defined as $q/2p'_0$, where $p'_0 = 100$ kPa, and the corresponding NL is used to compare the liquefaction resistance in this study. Firstly, compression in the vertical direction was applied and then the loading direction was reversed to extension when the target q, corresponding to the selected CSR, was achieved. The onset of liquefaction was determined when the double amplitude of axial strain (ε_{DA}) reached 2% and its calculation followed the JGS standard (Japanese Geotechnical Society Standard, 2016). During monotonic and cyclic loading, the CN and a were monitored. Following Thornton (2000), the mean mechanical coordination number (CN^*), that excludes the contribution from the non-active particles having $CNi < 2$, was computed as:

$$CN^* = 2\frac{N_c - N_c^{CNi<2}}{N_p - N_p^{CNi<2}} \quad (3)$$

where N_p is the total number of particles; CNi is the coordination number per particle. Following Otsubo et al. (2022), the mechanical void ratio (e^*) was calculated by counting the volume of non-active particles as the void volume. The CN_0^* and e_0^* values are listed in Tables 1 and 2.

4. Mechanical responses in monotonic loading

4.1. Drained monotonic loading

Drained monotonic compression and extension were applied separately up to ε_a of ±40%. Figs. 5a and 5b compare the overall and initial variations in q/p' for the *Iso-L*, *Ver-L*, and *Hor-L* samples. The *Ver-L* sample ($a_0 = 0.097$)

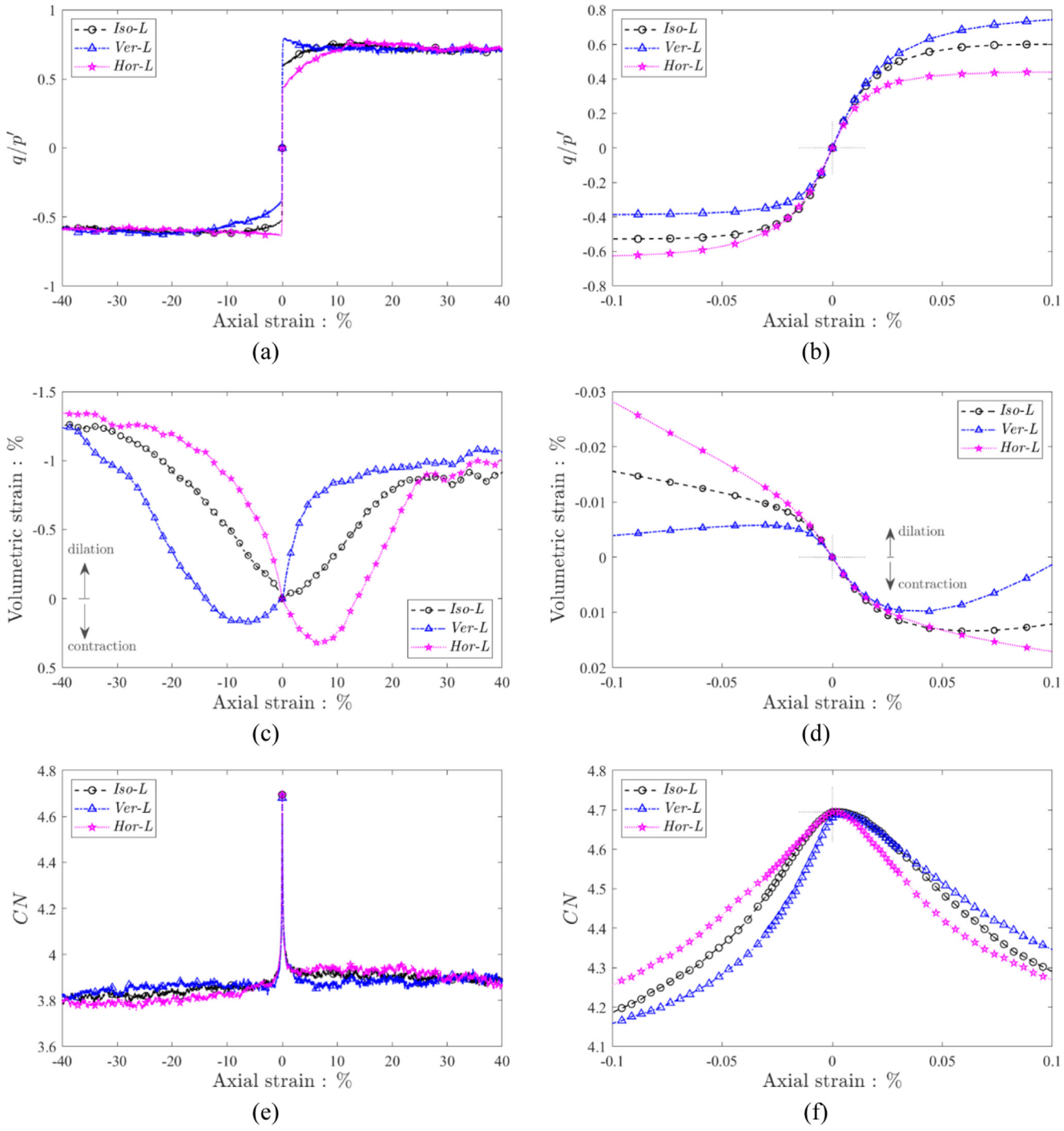

Fig. 5. Drained monotonic responses: (a) and (b) deviator stress ratio (q/p'), (c) and (d) volumetric strain (ε_{vol}), and (e) and (f) mean coordination number (CN) against axial strain. (a), (c), and (e) overall response and (b), (d), and (f) small-strain range.

shows a rapid growth in q/p' in compression ($\varepsilon_a > 0$), while the *Hor-L* sample ($a_0 = -0.098$) shows a stiffer response in extension ($\varepsilon_a < 0$). The *Iso-L* sample ($a_0 = -0.002$) gives an intermediate response on both sides. Their peak q/p' values vary measurably, but their residual q/p' values appear to be nearly identical. In contrast, Fig. 5c and 5d depict sensitive variations in ε_{vol}, where $\varepsilon_{vol} < 0$ corresponds to dilation. More dilative behaviour is observed for the *Ver-L* sample in compression and for the *Hor-L* sample in extension. The overall responses of q/p' and ε_{vol} with ε_a agree qualitatively with Yimsiri and Soga (2010). Referring to Figs. 5e and 5f, the *CN* of the *Hor-L* sample drops quickly in compression, while that of the *Ver-L* sample drops rapidly in extension. These initial variations (Fig. 5f) are closely related to the variations in q/p' (Fig. 5b), *i.e.*, a lower *CN* coincides with a lower magnitude of q/p' for a given ε_a.

4.2. Undrained monotonic loading

Referring to Fig. 6a for the undrained stress–strain relationship, the *Ver-L* and *Iso-L* samples show monotonic increases in q in compression, and the *Hor-L* and *Iso-L* samples show monotonic increases in the magnitude of q in extension. In contrast, the q for the *Hor-L* sample increases initially in compression followed by an abrupt decrease to $q = 0$ kPa, and then it increases again at around $\varepsilon_a = 16.2\%$; the *Ver-L* sample shows a similar response in extension. Referring to Fig. 6b for the effective stress paths, the contractive behaviour of the *Hor-L* sample in compression and the *Ver-L* sample in extension is evident, leading to a reduction in p' to zero. The lines toward the origin ($q = p' = 0$ kPa) are considered *instability lines*, and the state of zero effective stress is termed *static liquefaction* (Ishihara, 1993). A similar unstable response can be found in experiments for very loose sands (Yamamuro and Lade, 1997; Yoshimine and Ishihara, 1998). Huang et al. (2018) observed static liquefaction for loosely packed spherical particles in DEM even with an initially isotropic fabric.

Fig. 7 shows the initial responses of q and the *CN* up to ε_a of ±2%. The *Ver-L* sample is stiffer in compression while maintaining a relatively larger *CN*, whereas the *Hor-L* sample is stiffer in extension. The *CN* values for the *Hor-L* and *Ver-L* samples drop sharply at around +0.9% and −1.1%, respectively, corresponding to the points when q drops to zero (Fig. 7a). Referring to Fig. 8b, further loading leads to a gradual increase in the *CN* with visible fluctuations and then a sudden jump when the *CN* reaches around 3.65 ($CN^* \approx 4.35$). The *CN* values at ε_a of 40% are stable and identical among the three samples. At the ε_a of ±40%, the three samples are judged to have reached their critical states.

The overall variation in the *CN* is obviously different from the equivalent data for the drained monotonic loading case (Fig. 5e). The overall response of q/p' is similar regardless of the drainage conditions (Figs. 5a and 8a), but transient instability is observed for the undrained case due to the onset of static liquefaction. At the critical state, the effect of inherent anisotropy on q/p' or the *CN* appears insignificant; this agrees with the DEM results reported in the literature (Yimsiri and Soga, 2010; Dai et al., 2016).

4.3. Change in distribution of contact forces

A more sensitive variation is observed for the undrained monotonic case compared with the drained monotonic case in terms of q (Fig. 6). To visualise the development of stress transfer and contact forces, four stages in the undrained compression of the *Hor-L* sample (points a to d annotated in Figs. 6 to 8) were selected and compared in Fig. 9, and the following observations can be made.

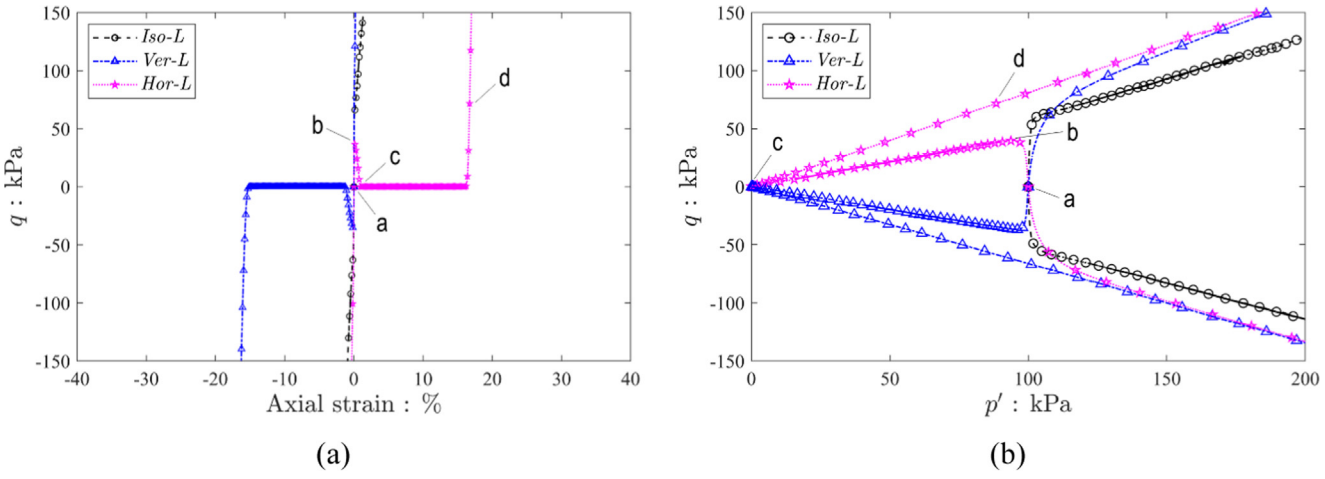

Fig. 6. Variations in (a) stress–strain relationship and (b) effective stress path during undrained monotonic loading.

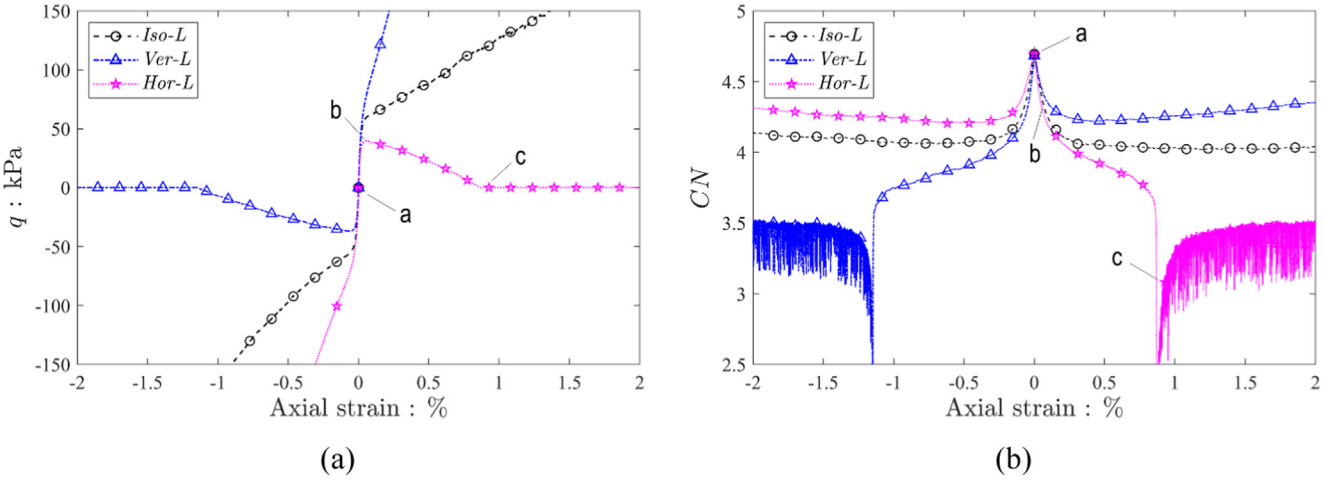

Fig. 7. Evolution of (a) deviator stress (q) and (b) mean coordination number (CN) within a small-strain range during undrained monotonic loading.

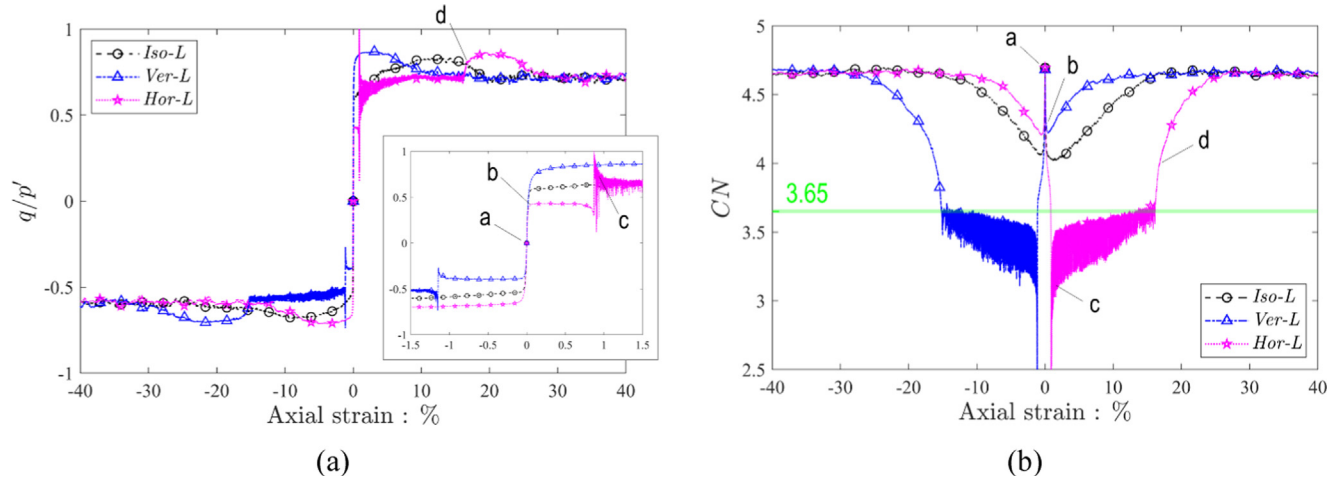

Fig. 8. Variations in (a) deviator stress ratio (q/p') and (b) mean coordination number (CN) with axial strain during undrained monotonic loading. The inset of Fig. 8a highlights the data points of the axial strain between −1.5% and 1.5%.

- Point a [$\varepsilon_a = 0\%$, $p' = 100$ kPa, $q = 0$ kPa, and $a = -0.098$] is the initial state where the distribution of contact forces is slightly biased in the horizontal direction (Fig. 4).
- Point b [$\varepsilon_a = 0.054\%$, $p' = 94.5$ kPa, $q = 39.7$ kPa, and $a = -0.014$] corresponds to the state where the temporary peak of q appears. The preferred direction of contact forces has become closer to the vertical.
- Point c [$\varepsilon_a = 0.928\%$, $p' \approx 0$ kPa, $q \approx 0$ kPa, and $a = 0.236$] is an unstable condition when both q and p' are almost zero, *i.e.*, static liquefaction, where $q/p' = 0.73$. Although the CN is 3.08 (Fig. 7b), a stable stress transfer is absent; each contact transfers negligible contact force, resulting in $p' \approx 0$ kPa.
- Point d [$\varepsilon_a = 16.7\%$, $p' = 88.4$ kPa, $q = 71.8$ kPa, and $a = 0.358$] is the point when p' recovers from zero and the CN has increased to 3.98. The vertical forces are dominant in this stage. This kind of recovery of p' after static liquefaction has rarely been documented in the literature, either in experiments or in DEM. This phenomenon is believed to occur due to the progressive rearrangement of the fabric, quantified by the CN or a, under constant volume conditions. This is discussed in further detail in Section 6.

5. Macroscopic response in undrained cyclic loading

5.1. Effect of CSR and inherent anisotropy

Fig. 10 compares the effect of the CSR on the *Iso-L* sample in terms of the stress–strain relationship and effective stress path. The CSR values of 0.15, 0.2, and 0.25 correspond to $q = \pm 30$, ± 40, and ± 50 kPa, respectively. A higher CSR causes a larger hysteresis per cycle in the stress–strain relationship and a profound reduction in p' in each cycle. With $CSR = 0.25$ (Fig. 10c), the sample reaches the zero effective stress condition, *i.e.*, *cyclic liquefaction*, in only several cycles. This kind of behaviour with

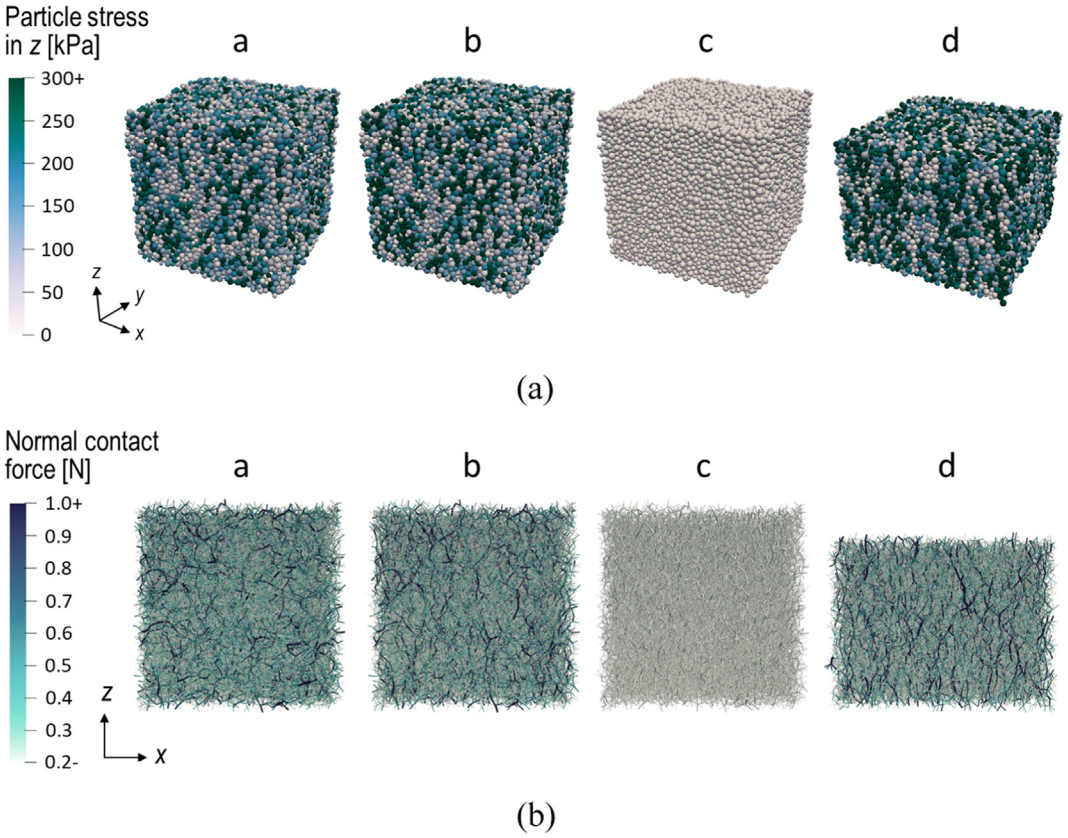

Fig. 9. Illustration of changes in (a) particle stress in z (vertical) direction and (b) normal contact force for *Hor-L* sample during undrained monotonic compression (points a, b, c, and d are annotated in Figs. 6 to 8).

limited deformation can be categorised as *cyclic mobility with limited flow* (Sze and Yang, 2014; Asadi et al. 2018).

The undrained cyclic responses of the *Ver-L* and *Hor-L* samples with $CSR = 0.15$ are depicted in Fig. 11. A greater axial strain develops in extension for the *Ver-L* sample, but an opposite trend is observed for the *Hor-L* sample. This trend is attributed to the initial anisotropic response in undrained monotonic loading. The *Ver-L* sample shows an unstable response toward cyclic liquefaction in extension (*i.e.*, $q < 0$) (Fig. 11a), while the *Hor-L* sample reaches cyclic liquefaction in compression (*i.e.*, $q > 0$) (Fig. 11b). A similar pattern of strain development, depending on the initial bedding angle, can be found in experiments (*e.g.*, Oda et al., 2001). This kind of unstable behaviour observed for the *Ver-L* and *Hor-L* samples can be categorised as *cyclic instability* (Castro, 1975).

Referring to the effective stress path in Fig. 11, when undrained monotonic and cyclic loading conditions are compared, the position of the instability line, denoted as *IL*, appears identical for a given sample. In addition, the effective stress path after the recovery of p' from zero, termed the *failure line* (*FL*), appears unique between monotonic loading and cyclic loading. This phenomenon is investigated in detail by comparing three different *CSR* values for the *Ver-L* sample in Fig. 12. The rate of reduction in p' per cycle depends on the magnitude of the *CSR*; however, the three cases eventually merge into an identical instability line followed by a failure line. A similar observation was reported by Huang et al. (2018) where loose DEM samples, having an initially isotropic fabric, were used. Yamada et al. (2010) also showed a similar agreement between undrained monotonic and cyclic loading in experiments. In this study, the *Iso-L* sample did not show static liquefaction; however, for the same density, the *Ver-L* and *Hor-L* samples exhibited static liquefaction (Fig. 6), leading to overall fragile responses during undrained cyclic loading. This observation qualitatively agrees with the experimental data in Tatsuoka et al. (1986) and Sze and Yang (2014) where a more isotropic fabric leads to a greater liquefaction resistance.

5.2. Effect of initial density

Compared to the *Iso-L* sample ($D_{r0} = 29.6\%$) with $CSR = 0.25$ (Fig. 10c), a more resilient response is observed for the *Iso-M* sample ($D_{r0} = 60.9\%$) (Fig. 13). This kind of behaviour – progressive deformation with an increasing number of load cycles – can be categorised as *cyclic mobility* (Castro, 1975; Vaid et al. 1985).

Figs. 14a and 14b show the responses of the *Iso-D* sample ($D_{r0} = 100\%$) at the 1st, 250th, and 500th cycles of loading. There is little change in its stress–strain relationship even at the 500th cycle (Fig. 14a). This implies that the densest packing is not prone to liquefaction due to no

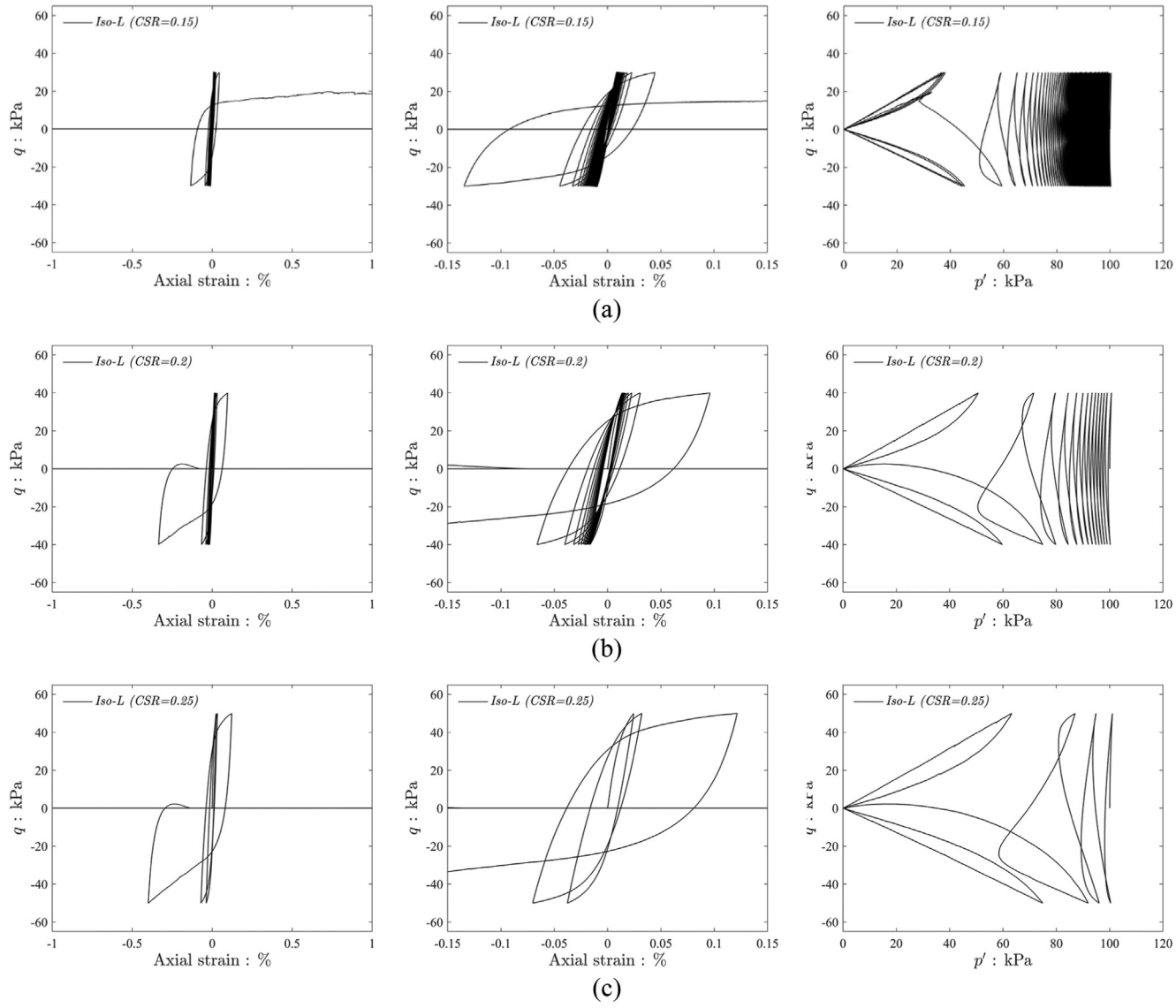

Fig. 10. Effect of *CSR* on stress–strain response and effective stress path of *Iso-L* sample for (a) $CSR = 0.15$, (b) $CSR = 0.2$, and (c) $CSR = 0.25$.

capacity for further contraction. Regarding the effective stress path, p' increases a little due to minor changes in the contact fabric and the creation of force chains (Fig. 14b). The same undrained cyclic loading was conducted using a face-centred cubic (*FCC*) packing having e_0 of 0.350, which is the densest packing of equally sized spheres; no change in the effective stress path is observed even at the 500th cycle (Fig. 14c).

Referring to Section 3.3, the onset of liquefaction was determined when ε_{DA} reached 2%, and the corresponding *NL* values were quantified. The *CSR*−*NL* relationships for all the tested samples are compared in Fig. 15. For loose samples ($D_{r0} \approx 30\%$), the curves for *Ver-L* and *Hor-L* are located below that for *Iso-L*. The effect of density on the *CSR*−*NL* relationship is obvious: a denser sample exhibits greater liquefaction resistance. Since the *Iso-D* sample did not show any reduction in p' at the 500th cycle, the arrows in Fig. 15 indicate that the actual *NL* should be >500.

5.3. Strain-dependent effect of inherent anisotropy

As discussed in Section 5.1, inherent anisotropy affects the deformation characteristics and liquefaction phenomena of granular materials. To understand the effect of a_0 on the liquefaction behaviour, the results for the *K*-series samples with various a_0 (Section 2.3, Table 2) were analysed.

Firstly, the initial shear moduli (G_0) of the *K*-series samples were quantified from the initial linear part (up to $\varepsilon_a = 0.001\%$) of the drained monotonic stress–strain relationship using the following formula:

$$G_0 = \frac{\Delta q}{2\Delta\varepsilon_q} \tag{4}$$

where $\Delta\varepsilon_q$ is the deviator strain, *i.e.*, the difference between the axial strain and the mean of the other two strain components. It is noteworthy that the initial slopes of the stress–strain curves up to $\varepsilon_a = \pm 0.001\%$ are identical

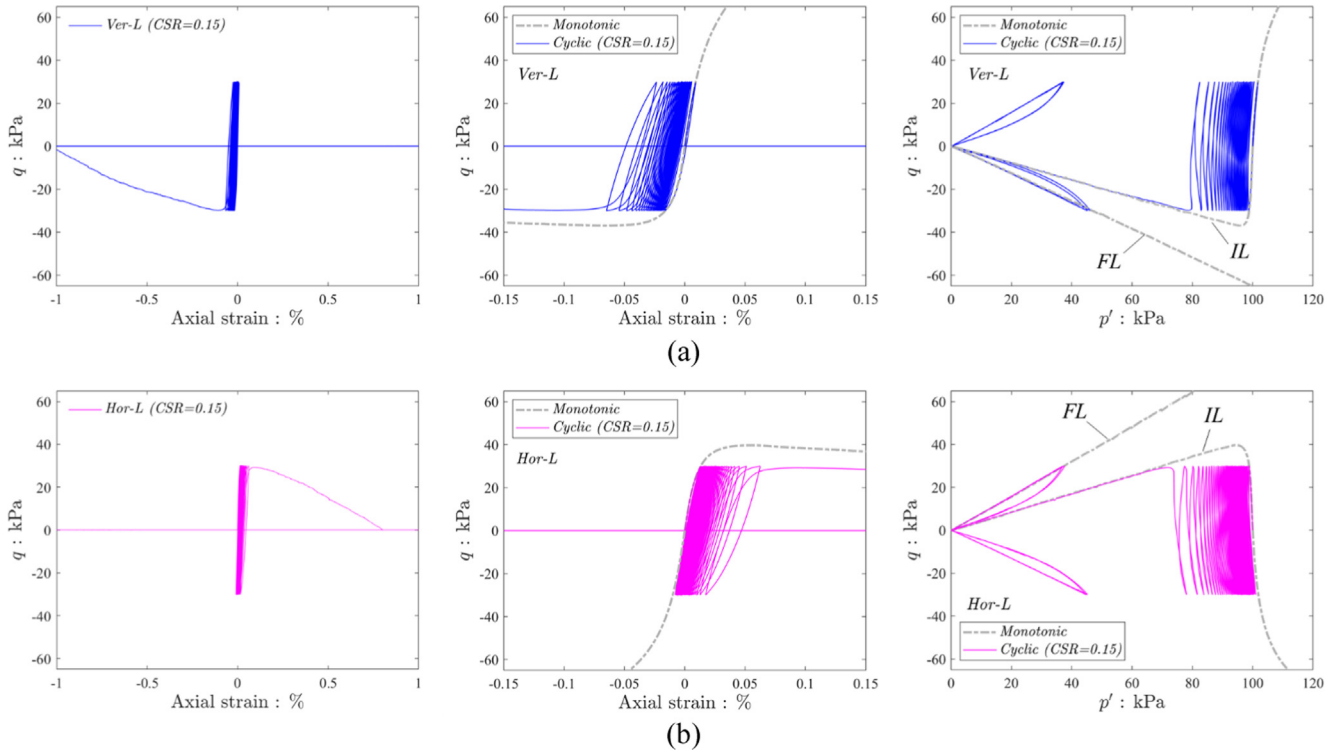

Fig. 11. Effect of initial fabric anisotropy on stress–strain relationship and effective stress path at $CSR = 0.15$ for (a) *Ver-L* sample and (b) *Hor-L* sample (*IL*: instability line, *FL*: failure line).

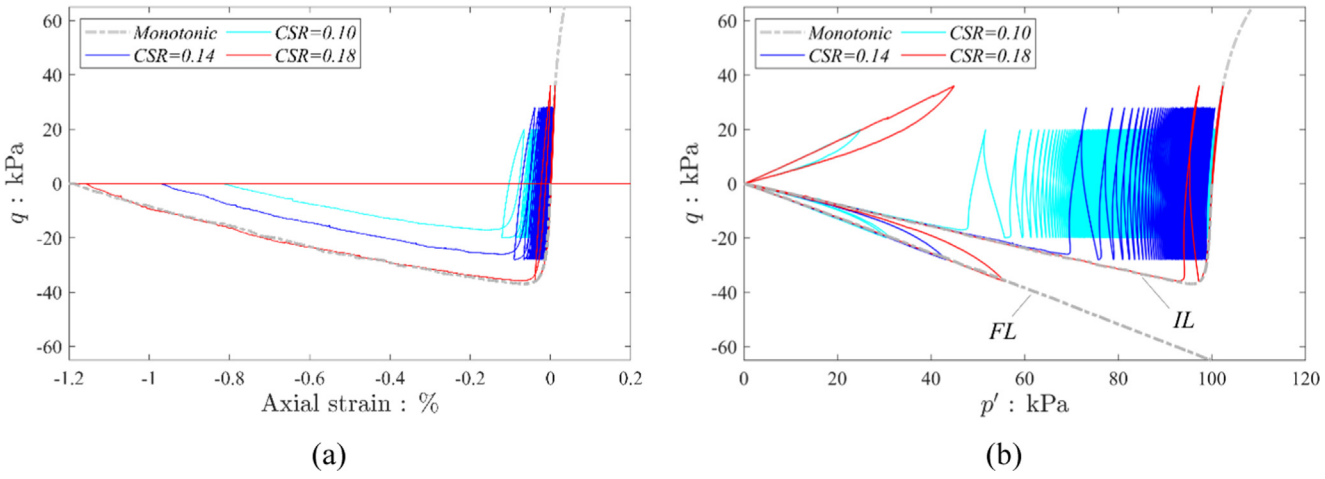

Fig. 12. Comparison of undrained monotonic and undrained cyclic responses at various *CSR* values for *Ver-L* sample: (a) stress–strain relationship and (b) effective stress path (*IL*: instability line, *FL*: failure line).

between compression and extension for the same sample (see Fig. 5b). Therefore, stiffness anisotropy was defined by comparing two stiffness components: vertically loaded and horizontally loaded (*i.e.*, G_{0v}/G_{0h}), as illustrated in Fig. 16a. The horizontally loaded stiffness was taken as the average stiffness when loaded in the *x*- and *y*-directions. G_{0v}/G_{0h} varies linearly with a_0 where the *K*1.00-*L* sample ($a_0 \approx 0$) gives almost isotropic stiffness (*i.e.*, $G_{0v}/G_{0h} \approx 1$).

Next, to understand how the stress–strain relationship evolves from elastic to plastic ranges under various a_0, the $q/p' - \varepsilon_a$ relationships for the *K*-series samples are plotted in Fig. 17a in which data points corresponding to $\varepsilon_a = \pm 0.005\%$ and $\pm 0.1\%$ are marked. Almost identical linear parts are observed within $\pm 0.005\%$, and then differences in the magnitude of q/p' become evident at $\varepsilon_a = \pm 0.1\%$. The q/p' values corresponding to $\varepsilon_a = \pm 0.005\%$ and ± 0.1 % are compared in Fig. 17b with respect to a_0.

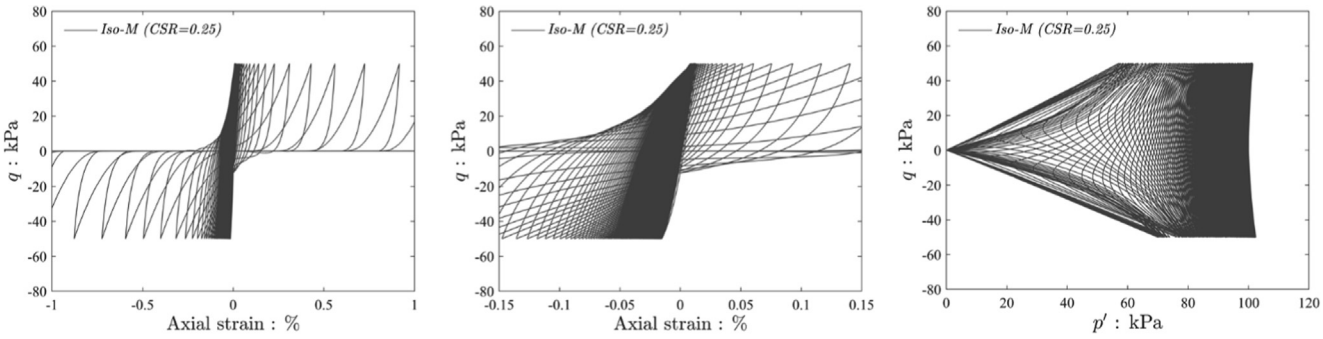

Fig. 13. Undrained cyclic responses of *Iso-M* sample ($D_{r0} = 60.9\%$): Stress–strain relationship and effective stress path at $CSR = 0.25$.

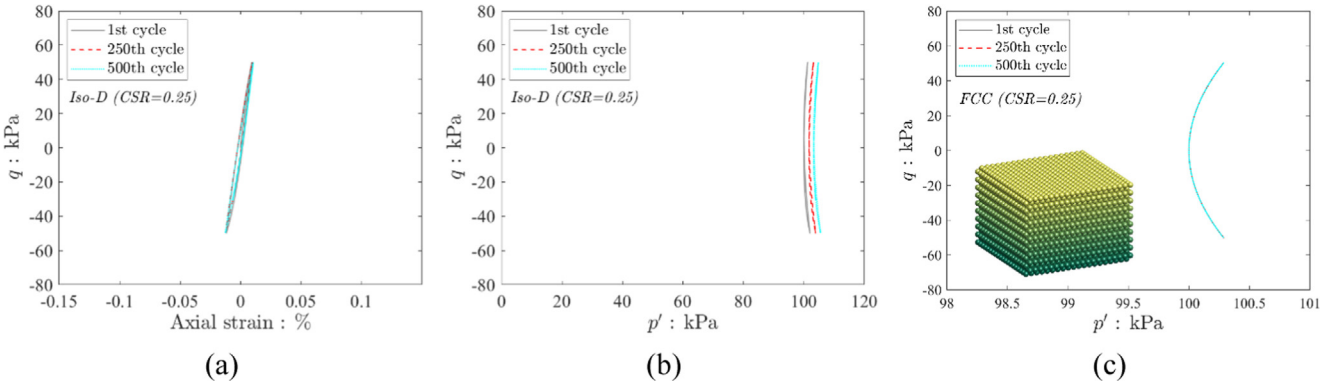

Fig. 14. Undrained cyclic responses of dense samples at $CSR = 0.25$: (a) stress–strain relationship, (b) effective stress path for *Iso-D* sample ($D_{r0} = 100\%$), and (c) effective stress path for *FCC* sample.

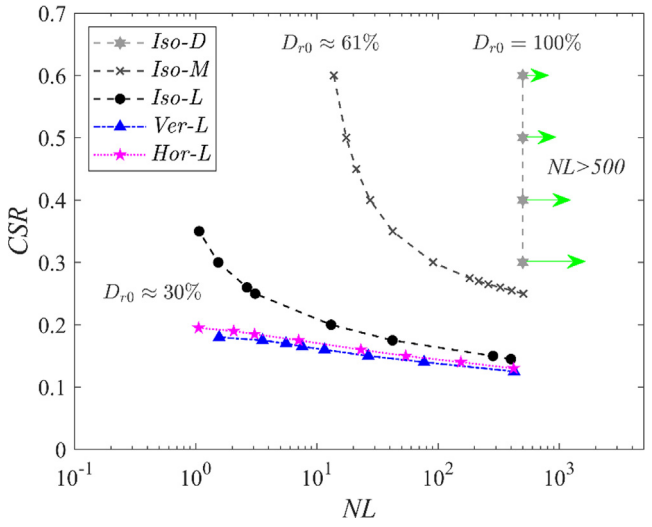

Fig. 15. Relationship between cyclic stress ratio (*CSR*) and number of cycles to liquefaction (*NL*) for *Iso*, *Ver*, and *Hor*-series samples ($CSR = q/2p'_0$; *NL* is determined when double amplitude axial strain exceeds 2% during undrained cyclic loading).

The effect of a_0 on q/p' appears to be linear and becomes significant by ±0.1 %.

Lastly, the $CSR-a_0$ relationships for the *K*-series samples are plotted in Fig. 16b with varying *CSR* values from 0.15 to 0.2. The *NL* is greater when a_0 is close to zero, and it decreases as the magnitude of a_0 increases. The following key observations are found based on the results of the *K*-series samples:

1. An insignificant variation in q/p' is found at the initial loading within $\varepsilon_a = \pm 0.005\%$ (Fig. 17a).
2. An increasing trend for q/p' with increasing a_0 is observed at $\varepsilon_a = \pm 0.1\%$ (Fig. 17b).
3. The variation in q/p' becomes less significant as loading continues beyond $\varepsilon_a = \pm 0.1\%$, which seems rational as the effect of a_0 on q/p' becomes minimal at the critical state (Fig. 8a).
4. Referring to Figs. 10 and 11, a decrease in p' occurs within $\varepsilon_a = \pm 0.1\%$ during undrained cyclic loading, indicating that the effect of inherent anisotropy on the *NL* is significant for the tested loose samples.
5. As discussed in Section 5.1, the samples having a larger degree of inherent anisotropy are more vulnerable to a particular direction of loading since their biased fabrics weaken rapidly during undrained cyclic loading. In contrast, samples having an isotropic fabric are potentially more resilient than those having higher or lower a_0, as evidenced in Figs. 15 and 16b.

It is noteworthy that the $NL-a_0$ relationship reported in Fig. 16b is obtained for samples with approximately the same CN_0 and e_0, and it is the a_0 that controls the variation

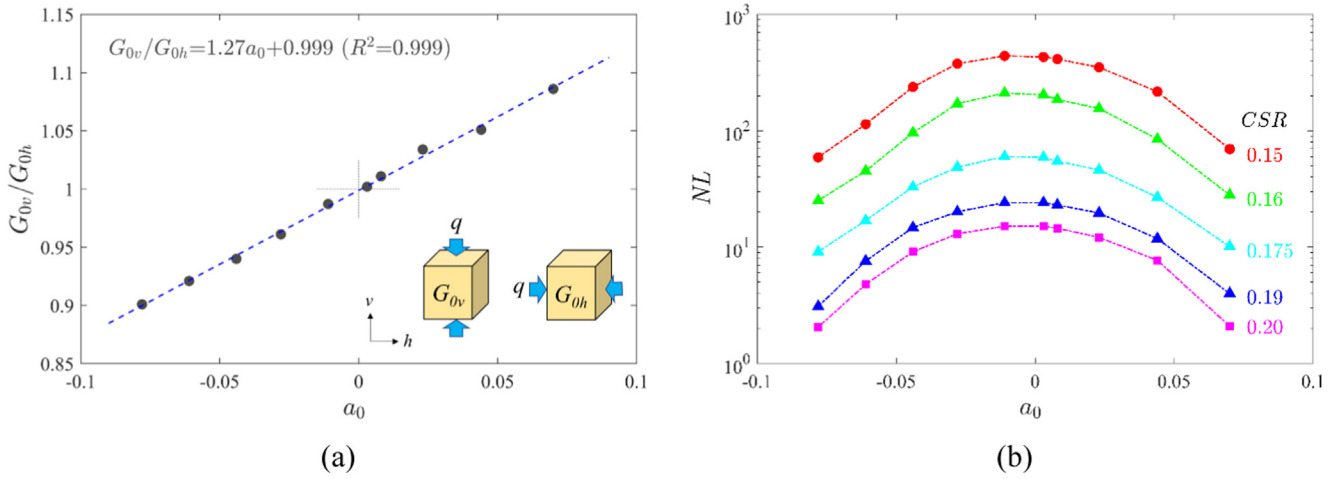

Fig. 16. Influence of initial anisotropic degree (a_0) on (a) stiffness anisotropy and (b) number of cycles to liquefaction (NL) at various CSR values for K-series samples (Table 2).

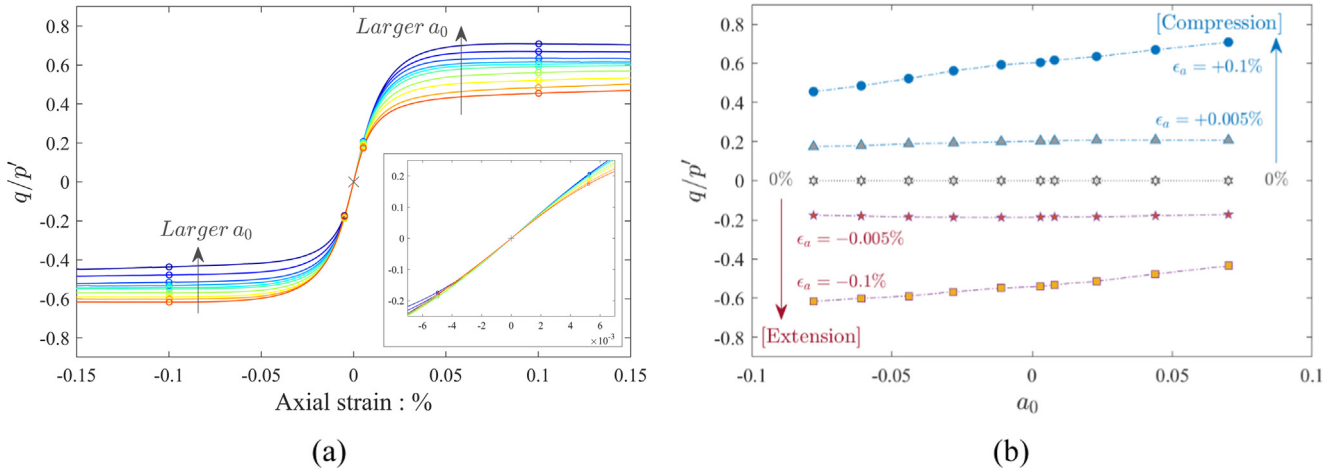

Fig. 17. Influence of initial anisotropic degree (a_0) on evolution of deviator stress ratio (q/p') during undrained monotonic loading: (a) stress–strain relationship and (b) q/p'–a_0 relationship for selected axial strain levels for K-series samples (Table 2). The inset of Fig. 17a highlights the data points of the axial strain between −0.007% and 0.007%.

in the NL. Wei and Wang (2017) reported a similar relationship among NL, CSR and a_0 (where $a_0 > 0$); however, their CN_0 values were also varied due to pre-shearing as a function of a_0 in their DEM simulations.

6. Evolution of fabric tensor and induced anisotropy

The influence of inherent anisotropy on the macroscopic mechanical response during undrained cyclic loading was discussed in Section 5. This section investigates the contact-scale microscopic responses, focusing on the variations in the CN and a using the *Iso-L*, *Ver-L*, and *Hor-L* samples.

6.1. Variation in CN during undrained cyclic loading

Figs. 18a and 18b display the evolution of the CN during undrained cyclic loading with $CSR = 0.15$ in terms of the accumulated axial strain ($\sum|\varepsilon_a|$) and ε_a, respectively. The three samples have $CN_0 \approx 4.7$ at their initial states (Table 1) and maintain similar values at the beginning of cyclic loading, annotated as pre-liquefaction in Fig. 18. Cyclic liquefaction takes place when the CN drops to 0 where the granular materials are unstable. In contrast, the CN does not reach zero (Fig. 8b) during static liquefaction. In Fig. 18, the CN increases gradually to around 3.65 and then drops to 0 once again; the drop in the CN occurs repeatedly whenever the loading direction is reversed after q recovers to the target CSR. The threshold CN of around 3.65 ($CN^* \approx 4.35$) appears to be equivalent to that for undrained monotonic loading (Fig. 8b). Even after a large $\sum|\varepsilon_a|$ value has developed, the threshold CN is maintained (Fig. 18a). A similar pattern for the variations in CN^* was observed in this study; the data are not shown here for conciseness. The threshold CN is lower than CN_0, probably due to the lower p' at the load reversal points

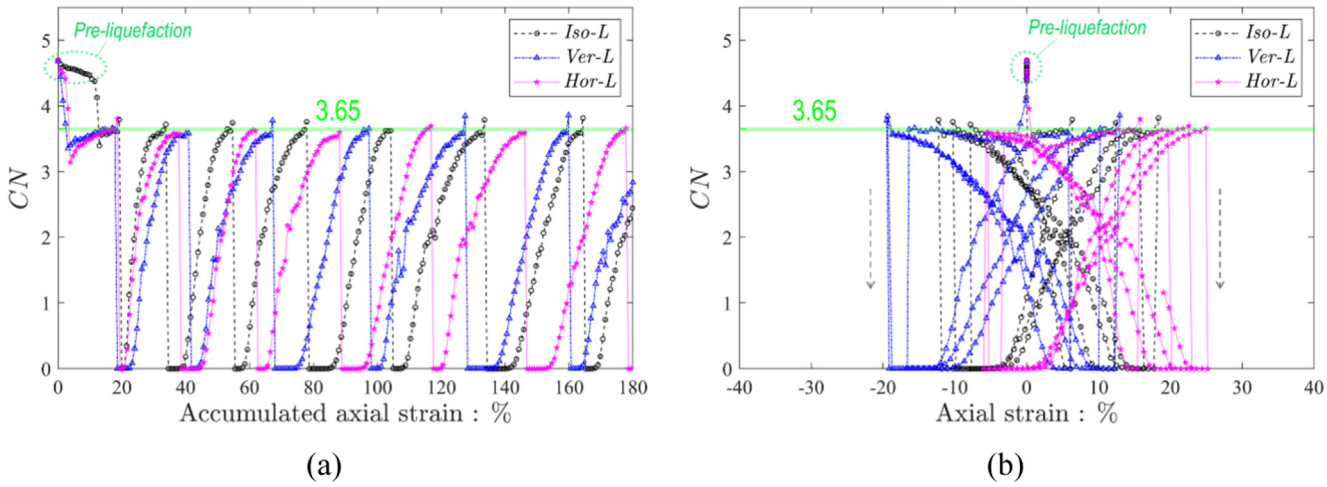

Fig. 18. Evolution of mean coordination number (CN) during undrained cyclic loading at $CSR = 0.15$ against (a) accumulated axial strain and (b) axial strain.

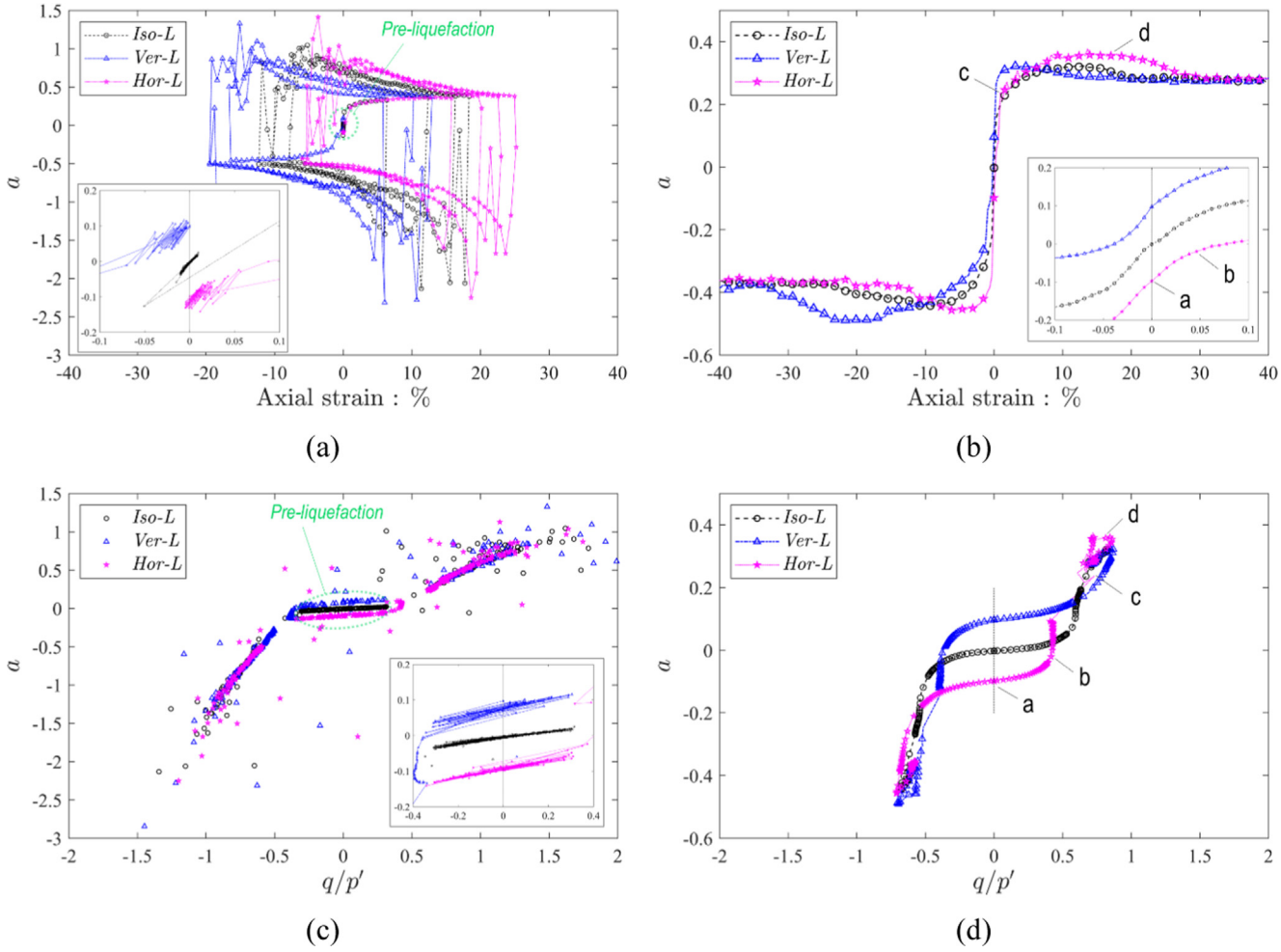

Fig. 19. Variations in anisotropic degree (a) with (a) axial strain under undrained cyclic loading at $CSR = 0.15$, (b) axial strain under undrained monotonic loading, (c) deviator stress ratio under undrained cyclic loading at $CSR = 0.15$, and (d) deviator stress ratio under undrained monotonic loading. The insets of Figs. 19a, 19b, and 19c highlight the data points at the initial part of the loading.

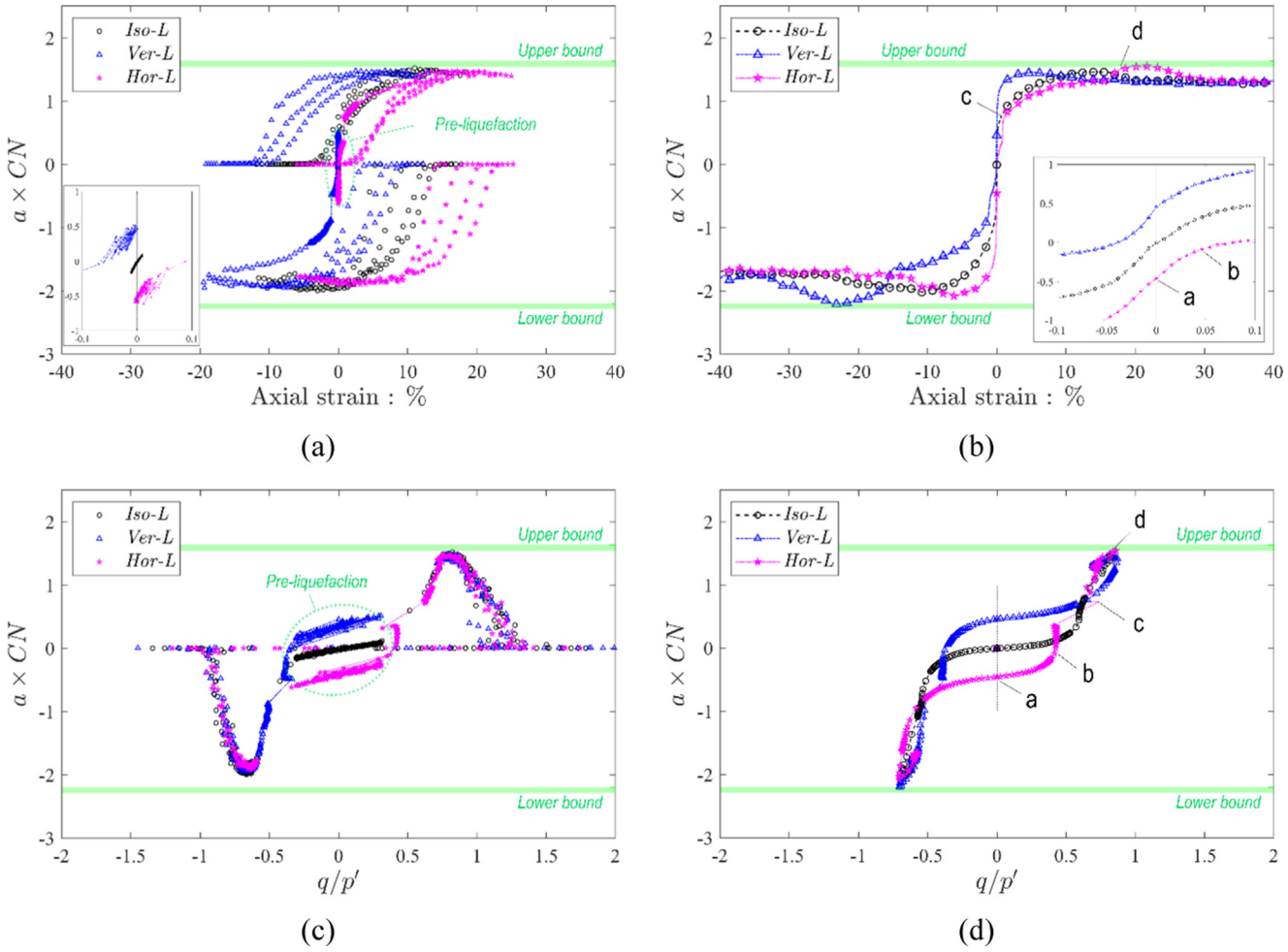

Fig. 20. Variations in effective anisotropy ($a \times CN$) with (a) axial strain under undrained cyclic loading at $CSR = 0.15$, (b) axial strain under undrained monotonic loading, (c) deviator stress ratio under undrained cyclic loading at $CSR = 0.15$, and (d) deviator stress ratio under undrained monotonic loading. The insets of Figs. 20a and 20b highlight the data points at the initial part of the loading.

as well as the shear history accumulated during cyclic loading.

Furthermore, Fig. 18b indicates that the range in axial strain attained during cyclic liquefaction is affected by the inherent anisotropy where the *Hor-L* sample accumulates axial strain on the compression side, while the *Ver-L* sample exhibits an opposite trend. This makes sense as samples tend to deform more in their weaker directions during undrained cyclic loading depending on their inherent anisotropy (Fig. 11). This indicates that the residual axial strain after the onset of cyclic liquefaction may vary depending on inherent anisotropy. A recent DEM simulation by Wei et al. (2018) showed a similar influence of inherent anisotropy induced by pre-shearing.

6.2. Evolution of induced anisotropy

An analysis using the *CN* alone cannot capture the change in fabric anisotropy during loading. Therefore, the evolution of a, *i.e.*, induced anisotropy, was quantified. Figs. 19a and 19b illustrate the evolution of a with ε_a during undrained cyclic loading with $CSR = 0.15$ and monotonic loading, respectively. Figs. 19c and 19d show the variation in a in terms of q/p'. There is no systematic pattern for the variation in a during undrained cyclic loading where the response changes drastically between pre-liquefaction and during cyclic liquefaction. Similar observations during cyclic liquefaction were reported in Wang and Wei (2016), confirming that this kind of complicated phenomenon can be observed in granular materials. In contrast, the variation in a during undrained monotonic loading is more stable and systematic. The overall variation in a during undrained monotonic loading, shown in Figs. 19b and 19d, is similar to that presented in Yimsiri and Soga (2010).

It is clear from Figs. 19a and 19c that the magnitude of a exceeds 1.0 during cyclic liquefaction, which is one order of magnitude higher than the range in a_0 investigated in this study. The possible range in a is -5.0 to 1.67 according to Eq. (2). It is also noted that, soon after the loading direction is reversed, the sign of a is reversed and the magnitude of a exceeds the range in a_0; this observation implies that

the soil fabric only momentarily recovers an isotropic state during cyclic liquefaction. A sample having initial anisotropy tends to deform more in its weaker direction, and thus, exhibits a lower liquefaction resistance. Therefore, extremely anisotropic fabric with a larger magnitude of a, when q recovers to the target CSR during cyclic liquefaction, is deemed to be quite unstable when loaded in the reverse direction: the CN drops to almost zero immediately after the load reversal (Fig. 18).

6.3. Alternative index – Effective anisotropy

A possible explanation for the different trends in a between the two loading conditions is that the CN drops to almost zero when the loading direction is reversed during cyclic liquefaction (Fig. 18). Therefore, a small number of contacts determine a, which does not represent the overall state of the fabric. This contribution proposes an alternative index, termed *effective anisotropy*, as the product of a and CN, *i.e.*, $a \times CN$, so that the evolution of induced anisotropy can be tracked effectively and compared systematically between the two loading conditions. Similar indices, $\varphi_v \times CN$ and $\varphi_h \times CN$, have been used by Li et al. (2021) for drained monotonic compression. Fig. 20 depicts the variation in $a \times CN$ in terms of ε_a or q/p' to be compared with Fig. 19. Fig. 20 shows horizontal lines indicating the upper and lower bounds of $a \times CN$, taken from the highest and lowest values, respectively, in the undrained monotonic loading tests. It is noteworthy that the magnitude of $a \times CN$ in the cyclic loading test depends on the selected CSR; setting an infinitely large CSR makes the cyclic loading test equivalent to the monotonic loading test. The threshold effective anisotropy is one of the material characteristics for the given samples irrespective of the loading types under undrained conditions. It should be noted that the threshold $a \times CN$ values depend on e_0, PSD, and the drainage conditions.

7. Limitations of this contribution

This study lacks several important aspects of granular soil, *e.g.*, particle shape, PSD, and degree of saturation. Recent DEM simulations have used multi-sphere clumps to represent non-spherical particles (*e.g.*, Katagiri, 2019; Angelidakis et al., 2021). It is likely that factors, such as particle shape parameters and major axis orientation, will contribute to the mechanical response. PSD influences the attainable ranges in the e and CN values (Liu et al., 2021). The tested range in a_0 for the loose samples in Tables 1 and 2 covers extremely anisotropic conditions under the specific e_0 and CN_0 adopted in this study; however, this range would be altered if the particle shape or PSD were different. The effect of partial saturation is not considered in this study. However, in experiments, the degree of saturation is critical for liquefaction resistance as the excess pore water pressure does not develop rapidly (*e.g.*, Okamura and Soga, 2006; Mele et al., 2019). Kuhn and Daouadji (2020) focused on this effect using DEM. Lastly, the present DEM analysis is limited to triaxial testing conditions. Recently, Jiang et al. (2021) compared the dynamic response of spherical particles using DEM under horizontally polarised shear- and Love-wave strain conditions. While acknowledging the above limitations, this study nonetheless provides the essential mechanical responses of granular materials subjected to both monotonic and cyclic loading influenced by inherent anisotropy.

8. Conclusions

This contribution investigated the effect of inherent anisotropy, *i.e.*, initial soil fabric, on the mechanical response of granular materials subjected to drained/undrained monotonic loading and undrained cyclic loading using DEM in relation to their induced anisotropy. For this purpose, the initial anisotropic degree, a_0, was varied systematically for samples with approximately the same e_0 and initial mean coordination number, CN_0. Based on systematic analyses using spherical particles, the following conclusions can be drawn:

- The initial stiffness and peak strength of anisotropic samples will be greater if compression is applied in the direction of the preferred contact normals. For example, a sample having a similar fabric to those prepared by the air-pluviation method tends to exhibit a greater resistance to compression compared to extension.
- The influence of a_0 on the development of q/p' during drained monotonic loading is considerable at small to medium strain levels, whereas its effect is insignificant at the residual state ($\varepsilon_a = \pm 40\%$).
- The overall response of q/p' against axial strain appears to be similar between drained and undrained monotonic loading tests.
- During undrained monotonic loading, variations in q and the CN appear sensitive to a_0 compared to drained monotonic loading. For the *Ver-L* and *Hor-L* samples, instability followed by static liquefaction was observed in the weakly structured direction. However, a recovery of p' took place during further monotonic loading at a larger strain level; consequently, the q/p' and CN at the residual state became independent of a_0.
- The liquefaction resistance curve, *i.e.*, the $CSR-NL$ relationship, is found to depend not only on D_{r0}, but also on a_0. A sample having a large degree of anisotropy tends to deform more in its weaker direction at an early stage of undrained cyclic loading, leading to a lower NL, compared to samples having an isotropic fabric. Thus, the presence of inherent anisotropy tends to reduce the liquefaction resistance of granular materials composed of spherical particles.

- Extremely anisotropic fabric with a larger magnitude of a, when q recovers to the target CSR during cyclic liquefaction, is deemed to be quite unstable when loaded in the reverse direction: the CN drops to almost zero immediately after the load reversal.
- Microscopic analyses revealed the presence of a threshold CN at which p' recovers from zero after static liquefaction (Fig. 8b) and cyclic liquefaction (Fig. 18). This threshold CN is around 3.65 ($CN^* \approx 4.35$) for the tested material and conditions in this study, regardless of monotonic or cyclic loading.
- There is no systematic pattern of changes in a during undrained monotonic and cyclic loading since the CN varies significantly where the CN drops to almost zero during cyclic liquefaction. An alternative new index proposed in this study, effective anisotropy ($a \times CN$), can be used when the two loading conditions are compared in terms of induced anisotropy, which provides similar upper and lower bounds irrespective of the loading conditions.

Acknowledgements

This work was supported by JSPS KAKENHI Grant Number JP20K20538. The research was conducted using Fujitsu PRIMERGY CX400M1/CX2550M5 (Oakbridge-CX) in the Information Technology Center of The University of Tokyo.

References

Angelidakis, V., Nadimi, S., Otsubo, M., Utili, S., 2021. CLUMP: A Code Library to Generate Universal Multi-sphere Particles. SoftwareX 15. https://doi.org/10.1016/j.softx.2021.100735 100735.

Asadi, M.S., Asadi, M.B., Orense, R.P., Pender, M.J., 2018. Undrained cyclic behavior of reconstituted natural pumiceous sands. J. Geotech. Geoenviron. Eng. 144 (8), 04018045. https://doi.org/10.1061/(ASCE)GT.1943-5606.0001912.

Bonilla, R.R.O., 2004. Numerical simulations of undrained granular media. University of Waterloo, Waterloo, ON, Canada.

Casagrande, A., 1976. Liquefaction and cyclic deformation of sands-a critical review. Harvard University, Cambridge, Massachusetts, Harvard Soil Mechanics Series, p. 88.

Castro, G., 1975. Liquefaction and cyclic mobility of saturated sands. Journal of the Geotechnical Engineering Division 101 (6), 551–569.

Chu, J., Leong, W.K., 2001. Pre-failure strain softening and pre-failure instability of sand: a comparative study. Géotechnique 51 (4), 311–321. https://doi.org/10.1680/geot.2001.51.4.311.

Dai, B., Yang, J., Zhou, C., Luo, X., 2016. DEM investigation on the effect of sample preparation on the shear behavior of granular soil. Particuology 25, 111–121. https://doi.org/10.1016/j.partic.2015.03.010.

Finn, W.D.L., Vaid, Y.P., 1977. Liquefaction potential from drained constant volume cyclic simple shear tests. In Proceedings of the 6th World Conference on Earthquake Engineering, New Delhi, India, 10–14.

Huang, X., Kwok, C., Hanley, K.J., Zhang, Z., 2018. DEM analysis of the onset of flow deformation of sands: linking monotonic and cyclic undrained behaviours. Acta Geotech. 13, 1061–1074. https://doi.org/10.1007/s11440-018-0664-3.

Ishibashi, I., Capar, O.F., 2003. Anisotropy and its relation to liquefaction resistance of granular material. Soils Found. 43 (5), 149–159. https://doi.org/10.3208/sandf.43.5_149.

Ishihara, K., 1993. Liquefaction and flow failure during earthquakes. Géotechnique 43 (3), 351–451. https://doi.org/10.1680/geot.1993.43.3.351.

Ishihara, K., Koga, Y., 1981. Case studies of liquefaction in the 1964 Niigata earthquake. Soils Found. 21 (3), 35–52. https://doi.org/10.3208/sandf1972.21.3_35.

Japanese Geotechnical Society Standard, 2016. Method for cyclic undrained triaxial test on soils (JGS 0541-2009). Laboratory Testing Standards of Geomaterials Vol. 2.

Jiang, M., Kamura, A., Kazama, M., 2021. Comparison of liquefaction behavior of granular material under SH- and Love-wave strain conditions by 3D DEM. Soils Found. 61 (5), 1235–1250. https://doi.org/10.1016/j.sandf.2021.06.013.

Katagiri, J., 2019. A novel way to determine number of spheres in clump-type particle-shape approximation in discrete-element modelling. Géotechnique 69 (7), 620–626. https://doi.org/10.1680/jgeot.18.P.021.

Kuhn, M.R., Daouadji, A., 2020. Simulation of undrained quasi-saturated soil with pore pressure measurements using a discrete element (DEM) algorithm. Soils Found. 60 (5), 1097–1111. https://doi.org/10.1016/j.sandf.2020.05.013.

Li, Y., Otsubo, M., Kuwano, R., 2021. DEM analysis on the stress wave response of spherical particle assemblies under triaxial compression. Comput. Geotech. 133. https://doi.org/10.1016/j.compgeo.2021.104043 104043.

Liu, D., O'Sullivan, C., Carraro, J., 2021. Influence of particle size distribution on the proportion of stress-transmitting particles and implications for measures of soil state. J. Geotech. Geoenviron. Eng. 147 (3), 04020182. https://doi.org/10.1061/(ASCE)GT.1943-5606.0002466.

Lopera Perez, J., Kwok, C., O'Sullivan, C., Huang, X., Hanley, K., 2016. Assessing the quasi-static conditions for shearing in granular media within the critical state soil mechanics framework. Soils Found. 56 (1), 152–159. https://doi.org/10.1016/j.sandf.2016.01.013.

McCulloch, D.S., Bonilla, M.G., 1970. Effects of the earthquake of March 27, 1964, on the Alaska Railroad. US Government Printing Office, Washington, DC.

Mele, L., Tan Tian, J., Lirer, S., Flora, A., Koseki, J., 2019. Liquefaction resistance of unsaturated sands: experimental evidence and theoretical interpretation. Géotechnique 69 (6), 541–553. https://doi.org/10.1680/jgeot.18.P.042.

Miura, S., Toki, S., 1982. A sample preparation method and its effect on static and cyclic deformation-strength properties of sand. Soils Found. 22 (1), 61–77. https://doi.org/10.3208/sandf1972.22.61.

Monkul, M.M., Gültekin, C., Gülver, M., Akın, Ö., Eseller-Bayat, E., 2015. Estimation of liquefaction potential from dry and saturated sandy soils under drained constant volume cyclic simple shear loading. Soil Dyn. Earthquake Eng. 75, 27–36. https://doi.org/10.1016/j.soildyn.2015.03.019.

Morimoto, T., Otsubo, M., Koseki, J., 2021. Microscopic investigation into liquefaction resistance of pre-sheared sand: Effects of particle shape and initial anisotropy. Soils Found. 61 (2), 335–351. https://doi.org/10.1016/j.sandf.2020.12.008.

Ng, T.T., Dobry, R., 1994. Numerical simulations of monotonic and cyclic loading of granular soil. J. Geotech. Eng. 120 (2), 388–403. https://doi.org/10.1061/(ASCE)0733-9410(1994)120:2(388).

Ni, X., Ye, B., Zhang, F., Feng, X., 2021. Influence of specimen preparation on the liquefaction behaviors of sand and its mesoscopic explanation. J. Geotech. Geoenviron. Eng. 147 (2), 04020161. https://doi.org/10.1061/(ASCE)GT.1943-5606.0002456.

Oda, M., 1972. Initial fabrics and their relations to mechanical properties of granular material. Soils Found. 12 (1), 17–36. https://doi.org/10.3208/sandf1960.12.17.

Oda, M., 1982. Fabric tensor for discontinuous geological materials. Soils Found. 22 (4), 96–108. https://doi.org/10.3208/sandf1972.22.4_96.

Oda, M., Kawamoto, K., Suzuki, K., Fujimori, H., Sato, M., 2001. Microstructural interpretation on reliquefication of saturated granular soils under cyclic loading. J. Geotech. Geoenviron. Eng. 127 (5), 416–423. https://doi.org/10.1061/(ASCE)1090-0241(2001)127:5(416).

Okamura, M., Soga, Y., 2006. Effects of pore fluid compressibility on liquefaction resistance of partially saturated sand. Soils Found. 46 (5), 695–700. https://doi.org/10.3208/sandf.46.695.

Otsubo, M., O'Sullivan, C., Shire, T., 2017. Empirical assessment of the critical time increment in explicit particulate discrete element method simulations. Comput. Geotech. 86, 67–79. https://doi.org/10.1016/j.compgeo.2016.12.022.

Otsubo, M., Kuwano, R., O'Sullivan, C., Shire, T., 2022. Using geophysical data to quantify stress transmission in gap-graded granular materials. Géotechnique 72 (7), 565–582. https://doi.org/10.1680/jgeot.19.P.334.

Otsubo, M., 2016. Particle scale analysis of soil stiffness and elastic wave propagation. Ph.D. thesis, Imperial College London. https://doi.org/10.25560/44380.

Plimpton, S., 1995. Fast parallel algorithms for short-range molecular dynamics. J. Comput. Phys. 117 (1), 1–19. https://doi.org/10.1006/jcph.1995.1039.

Salot, C., Gotteland, P., Villard, P., 2009. Influence of relative density on granular materials behavior: DEM simulations of triaxial tests. Granular Matter 11 (4), 221–236. https://doi.org/10.1007/s10035-009-0138-2.

Sasaki, Y., Towhata, I., Miyamoto, K., Shirato, M., Narita, A., Sasaki, T., Sako, S., 2012. Reconnaissance report on damage in and around river levees caused by the 2011 off the Pacific coast of Tohoku earthquake. Soils Found. 52 (5), 1016–1032. https://doi.org/10.1016/j.sandf.2012.11.018.

Satake, M., 1982. Fabric tensor in granular materials. In: Vermeer, P.A., Luger, H.J. (Eds.), Deformation and Failure of Granular Materials. Balkema, Rotterdam, pp. 63–68.

Seed, H.B., Idriss, I.M., 1967. Analysis of soil liquefaction: Niigata earthquake. J. Soil Mech. Found. Div. 93 (3), 83–108.

Seed, H.B., Lee, K.L., 1966. Liquefaction of saturated sands during cyclic loading. J. Soil Mech. Found. Div. 92 (6), 105–134.

Suzuki, T., Suzuki, T., 1988. Effects of density and fabric change on reliquefaction resistance of saturated sand. Soils Found. 28 (2), 187–195. https://doi.org/10.3208/sandf1972.28.2_187, in Japanese.

Sze, H.Y., Yang, J., 2014. Failure modes of sand in undrained cyclic loading: impact of sample preparation. J. Geotech. Geoenviron. Eng. 140 (1), 152–169. https://doi.org/10.1061/(ASCE)GT.1943-5606.0000971.

Tatsuoka, F., Ochi, K., Fujii, S., Okamoto, M., 1986. Cyclic undrained triaxial and torsional shear strength of sands for different sample preparation methods. Soils Found. 26 (3), 23–41. https://doi.org/10.3208/sandf1972.26.3_23.

Thornton, C., 2000. Numerical simulations of deviatoric shear deformation of granular media. Géotechnique 50 (1), 43–53. https://doi.org/10.1680/geot.2000.50.1.43.

Vaid, Y.P., Chern, J.C., Tumi, H., 1985. Confining pressure, grain angularity, and liquefaction. J. Geotech. Eng. 111 (10), 1229–1235. https://doi.org/10.1061/(ASCE)0733-9410(1985)111:10(1229).

Vaid, Y.P., Sivathayalan, S., Stedman, D., 1999. Influence of specimen-reconstituting method on the undrained response of sand. Geotech. Test. J. 22 (3), 187.

Wang, G., Wei, J., 2016. Microstructure evolution of granular soils in cyclic mobility and post-liquefaction process. Granular Matters 18, 51. https://doi.org/10.1007/s10035-016-0621-5.

Wei, J., Wang, G., 2017. Discrete-element method analysis of initial fabric effects on pre- and post-liquefaction behavior of sands. Géotech. Lett. 7 (2), 161–166. https://doi.org/10.1680/jgele.16.00147.

Wei, J., Huang, D., Wang, G., 2018. Microscale descriptors for particle-void distribution and jamming transition in pre- and post-liquefaction of granular soils. J. Geotech. Geoenviron. Eng. 144 (8), 04018067. https://doi.org/10.1061/(ASCE)EM.1943-7889.0001482.

Yamada, S., Takamori, T., Sato, K., 2010. Effects on reliquefaction resistance produced by changes in anisotropy during liquefaction. Soils Found. 50 (1), 9–25. https://doi.org/10.3208/sandf.50.9.

Yamamuro, J.A., Lade, P.V., 1997. Static liquefaction of very loose sands. Can. Geotech. J. 34 (6), 905–917. https://doi.org/10.1139/t97-057.

Yamashita, S., Toki, S., 1993. Effects of fabric anisotropy of sand on cyclic undrained triaxial and torsional strengths. Soils Found. 33 (3), 92–104. https://doi.org/10.3208/sandf1972.33.3_92.

Yang, Z.X., Li, X.S., Yang, J., 2008. Quantifying and modelling fabric anisotropy of granular soils. Géotechnique 58 (4), 237–248. https://doi.org/10.1680/geot.2008.58.4.237.

Yimsiri, S., Soga, K., 2010. DEM analysis of soil fabric effects on behaviour of sand. Géotechnique 60 (6), 483–495. https://doi.org/10.1680/geot.2010.60.6.483.

Yoshimine, M., Ishihara, I., 1998. Flow potential of sand during liquefaction. Soils Found. 38 (3), 189–198. https://doi.org/10.3208/sandf.38.3_189.